MAGNETIC RESONANCE STUDY OF POINT DEFECTS IN $KMgF_3$ AND $RbMgF_3$

By

KANAN BIHARI SAHA

Bachelor of Science
University of Calcutta
Calcutta, India
1960

Master of Science
University of Calcutta
Calcutta, India
1962

Master of Science in Physics
Cleveland State University
Cleveland, Ohio
1972

Submitted to the Faculty of the Graduate College
of the Oklahoma State University
in partial fulfillment of the requirements
for the Degree of
DOCTOR OF PHILOSOPHY
July, 1978

MAGNETIC RESONANCE STUDY OF POINT DEFECTS

IN $KMgF_3$ AND $RbMgF_3$

Thesis Approved:

Larry E. Hallibrton
Thesis Adviser

J Paul Devlin

Joel J Martin

Norman N Durham
Dean of the Graduate College

ACKNOWLEDGMENTS

The author wishes to thank Dr. L. E. Halliburton, major adviser, for his guidance and assistance throughout this entire investigation. Without his help, this work would never have been realized. Appreciation is expressed to Drs. W. A. Sibley, H. A. Pohl, P. A. Westhaus, E. E. Kohnke and J. J. Martin for many valuable suggestions and discussions. Thanks are also extended to Ms. Janet Sallee for typing this manuscript.

The author also wishes to express his appreciation to his wife for her continued encouragement throughout the course of this investigation.

Financial support from the National Science Foundation and the Physics Department at Oklahoma State University is gratefully acknowledged.

TABLE OF CONTENTS

LIST OF TABLES

LIST OF FIGURES

CHAPTER I

INTRODUCTION

Defects in crystal structures are known to cause many interesting effects in solid state science. The usefulness of semiconducting crystals is due to the presence of controlled amounts of different kinds of impurities in them. High energy radiation when incident on materials creates defects in them and the electronic structures of these defects depend upon the types of material (i.e., ionic, covalent, metallic). These radiation-induced defects endow the crystal with properties very different from the material's intrinsic properties and investigation of these point defects sheds light on some fundamental processes that occur in matter.

The technological importance of such investigations cannot be over emphasized. Structural materials in nuclear reactors are exposed to intense radiation fields. A thorough understanding of radiation-induced defects is thus important in selecting structural materials. Instruments aboard a spaceship are exposed to varied kinds of radiation of extra-terrestrial origin. Knowledge of radiation-induced defects is essential in evaluating the performance of these electronic components.

The data available on the effects of radiation on materials in a wide variety of environments is quite vast. But even then a thorough understanding of the electronic structures and production criteria of such simple defects as F centers in ionic materials has yet to be ac-

quired. In monovalent ionic crystals such as alkali halides, an F center consists of a single electron trapped at a negative ion vacancy and in perhaps the simplest of all point defects. Because of its simplicity the F center provides the best hope of developing a thorough understanding of a particular defect and thus it is most often studied.

In the investigation described in this dissertation, the study of F centers has been extended to the cubic perovskite crystal structure. The interactions of the F center electron with neighboring magnetic nuclei have been determined in $KMgF_3$ by using the electron nuclear double resonance (ENDOR) technique. A characterization of the intrinsic V_K center in $RbMgF_3$ by the electron spin resonance (ESR) technique is also reported here.

Previous F Center ENDOR Studies

F centers can be produced in ionic materials by irradiating with high energy photons (Y-ray, x-ray, UV) or with energetic electrons or neutrons. They can also be produced by electrolysis at high temperature or by heating the crystal in an alkal metal atmosphere (for alkali halide crystals). In this latter case, a stochiometric excess of alkali atoms is produced in the crystal and on quenching the crystal from high temperature one obtains F centers.

Production of F centers in ionic halogen crystals has been a subject of investigations for a long time. It is now generally believed that the photochemical damage process is operative in such materials. In the photochemical damage process creation of an F center results from an initial electronic excitation in the lattice. An incident high energy photon (Y-ray, x-ray, UV) creates an anion in an excited state. This is

represented by the following expression

$$X^- + h\nu \rightarrow X^{-*}$$

where X is a halogen. This excited anion then combines with another lattice anion to form a self trapped exciton.

$$X^{-*} + X^- \rightarrow X_2^{=*}$$

Of the several possible modes of decay of this exciton, the important ones are

$$X^{=*} \rightarrow 2X^- + \text{photon}, \tag{1}$$

$$X_2^{=*} \rightarrow 2X^- + \text{phonon}, \tag{2}$$

$$X_2^{=*} \rightarrow X_{int} + X^- + \text{F center}\ . \tag{3}$$

As can be seen from eqn. (3), creation of an F center is accompanied by the formation of an interstitial.

Since an F center (in a monovalent lattice) has an unpaired electron, it gives an ESR signal and additional detailed information about the F center can be obtained by using ENDOR. Structureless ESR lines of F centers are good examples of inhomogeneous broadening, a broadening that results from multiple hyperfine structure that can no longer be resolved in ESR. This hyperfine structure comes from the interaction of the F center electron with magnetic nuclei of different shells surrounding the F center. In alkali halides such as LiCl, LiBr, NaCl, NaBr, KF, KCl, KBr, KI, RbBr, and RbI the hyperfine structure is not resolved in the ESR spectra; each such ESR spectrum is a single structureless inhomo-

geneously broadened line.

For example, the linewidth of the ESR line of the F center in KCl is 47 gauss. In this latter case there will be 19 energy levels for the spin up case and 19 levels for the spin down case as a result of the interaction of the F center electron with the first shell potassium ^{39}K (I = 3/2, total effective spin for the combined first shell potassium nuclei is 9). Each of these 38 levels will be split into 37 additional energy levels as a result of interaction with the 12 chlorine nuclei in the second shell. Further splitting of each of these levels will occur because of interaction with nuclei of more distant shells. Because the linewidths of the individual transitions are greater than the energy separation between adjacent levels, a single broadened line results.

These unresolved hyperfine interactions can be determined by the ENDOR technique invented by Feher in 1956 (1). For KCl, hyperfine interaction constants of nuclei out to the eighth shell have been obtained through ENDOR measurements. As an example, a list of the hyperfine constants of F centers in KBr measured with ENDOR is given in Table I. Similar work has been done on F centers in other alkali halides (2,3,4, 5,6).

Very few ENDOR studies on F centers in materials other than the alkali halides have been done. ENDOR measurements on the first shell ^{25}Mg nuclei for F centers in MgO were made by Unruh and Culvahouse (7). Halliburton, et al. used the ENDOR technique to determine hyperfine interaction parameters of the F center electron with third and fifth shell ^{25}Mg nuclei in MgO (8). Unruh et al. completed an ENDOR study of the F center in MgF_2 (9).

TABLE I

HYPERFINE INTERACTION CONSTANTS OF THE F CENTER IN KBr OBTAINED THROUGH ENDOR

Shell	Nucleus	a/h (Mc)	b/h (Mc)
I	^{39}K	18.8	0.74
II	^{81}Br	42.8	2.7
III	^{39}K	0.27	0.022
IV	^{81}Br	5.70	0.41
V	^{39}K	0.16	0.02
VI	^{81}Br	0.83	0.086
VIII	^{81}Br	0.53	0.06

Previous V_K Center ESR Studies

Self trapped hole centers can be produced in ionic crystals by ionizing radiation at low temperatures. Formation of these V_K centers is facilitated by the presence of such impurities as Pb^{2+}, Tl^{+}, and Ag^{+} in the lattice, which act as electron traps. The ionizing radiation creates a hole on the lattice anion. This hole is then shared by another adjacent lattice anion forming a molecular ion (X_2^-)

$$X^- + h\nu \rightarrow X + e^-$$

$$X + X^- \rightarrow X_2^-$$

The V_K center is an electronic defect as opposed to the F center which is an ionic defect.

Känzig and co-workers (10, 11, 12, 13) x-irradiated crystals of alkali halides (LiF, NaCl, KCl, and KBr) and studied the electronic structure and orientation of the resulting self trapped hole centers. These studies showed that the V_K center is oriented along [110] axes of the crystals. These workers found large well-resolved hyperfine effects as a result of significant interaction with the two central halogen nuclei. In KCl, for example, they explained the relative intensities of the ESR lines in terms of the two isotopes of chlorine (^{35}Cl, ^{37}Cl) and showed that three different varieties of V_K centers were formed: XY^-, XX^-, and YY^-, where X and Y stand for ^{35}Cl and ^{37}Cl respectively. They also measured the g values.

Schoemaker (14) extended the earlier works of Känzig by making more detailed ESR studies of V_K centers in different alkali halides. His analysis shows that the isotropic part of the hyperfine interaction con-

stant decreases monotonically in going from the Rb to the Li salt, while the anisotropic part remains approximately constant. He also observed heteronuclear V_K type centers (i.e., Br-Cl^-) in doped samples.

Previous Work on $KMgF_3$ and $RbMgF_3$

A brief account of some of the investigations of radiation-induced point defects in $KMgF_3$ and $RbMgF_3$ are described in this section. $KMgF_3$ is a perovskite-structured polar crystal, and may be viewed as cubes with corners occupied by K^+ ions, body-centers occupied by Mg^{2+} ions and face-centers occupied by F^- ions (Figure 1).

Hall and Leggeat (15) x-irradiated a sample of $KMgF_3$ at room temperature and identified optical absorption bands due to F and M centers. They obtained a nine-line ESR spectrum for the F center, with a linewidth of about 50 gauss. They attributed the linewidth to unresolved hyperfine interactions with the four ^{39}K nuclei of the first shell. Harker (16) made a theoretical calculation of the electronic structure of the F center in $KMgF_3$ and predicted values for the hyperfine interaction constants of the nearest neighbour ^{25}Mg, ^{39}K, and ^{19}F nuclei with the ground state F center electron. Modine and Sonder (17) made a magnetic circular dichroism study of the F center in $KMgF_3$. Because of its intrinsic tetragonal symmetry, the F center should have ^2E_u and $^2A_{2u}$ excited states. However, their MCD spectra did not exhibit any such characteristics. They concluded that the state ^2E_u and $^2A_{2u}$ were either too close to be resolved or very widely separated in energy.

Young et al. irradiated a manganese-doped crystal of $KMgF_3$ at room temperature thereby obtaining Mn^{2+}-F center pairs (18). They observed that a subsequent UV bleaching at 77 K ionizes the F center electron

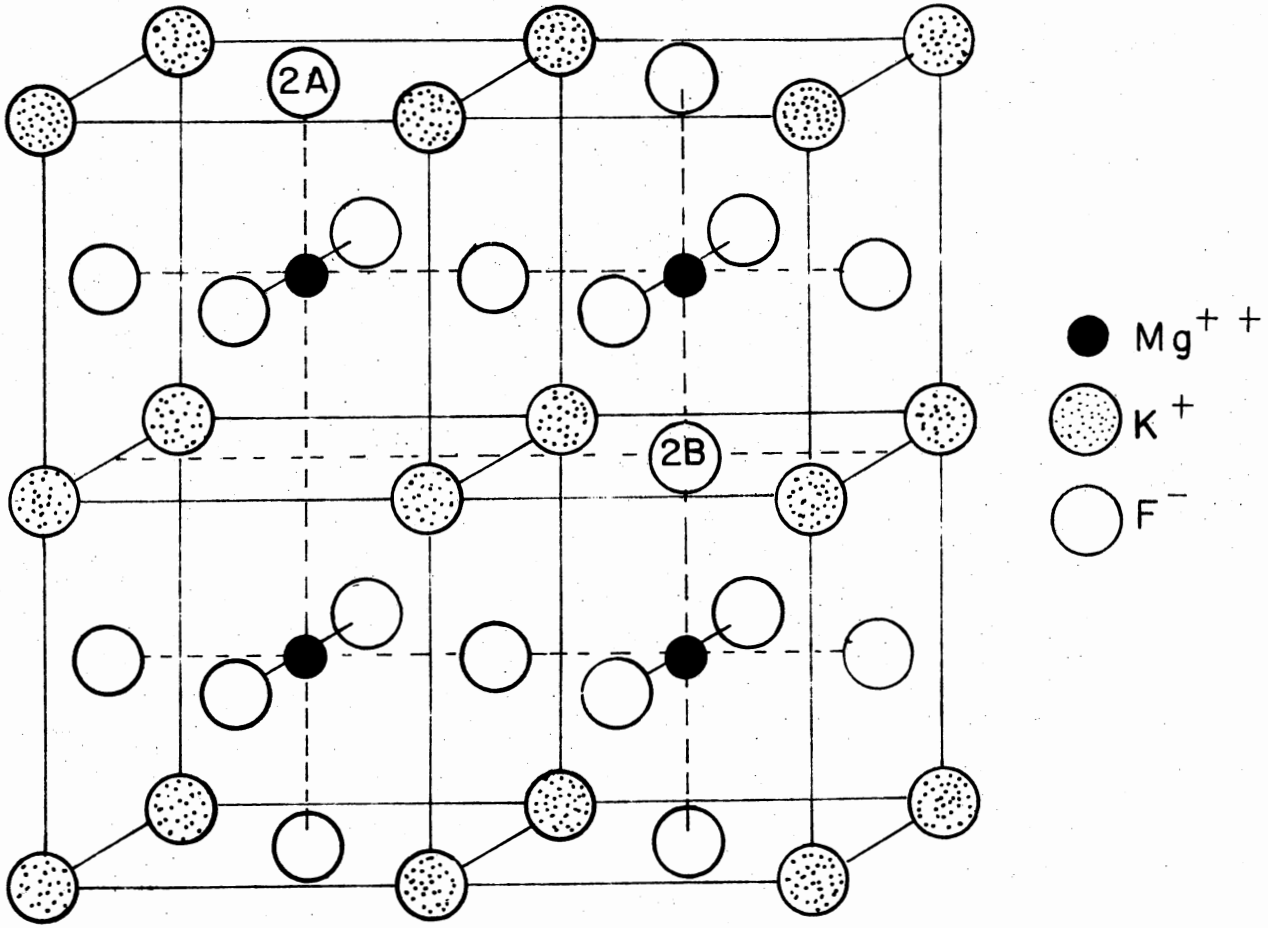

Figure 1. Crystal Structure of $KMgF_3$

leaving a Mn^{2+}-fluorine vacancy center. The ESR spectrum from this latter center was analyzed in detail. Optical absorption bands due to Mn^{2+}-F center pairs in $KMgF_3$:Mn have been identified by Lee (19).

Intrinsic self trapped hole centers in $KMgF_3$ have been well characterized using optical and ESR techniques (20, 21, 22). Hall (20) was the first to study V_K centers in $KMgF_3$. He observed that because of the low symmetry of anion pairs in the perovskite structure, none of the principal axes of the hyperfine tensors lie along the molecular axis thus reflecting the bent bond character of the molecular ion.

An electron spin resonance study of perturbed V_K centers in $KMgF_3$ has been made by Rhoads et al. (23). They have also made ESR investigations of intrinsic and perturbed fluorine interstitial centers in $KMgF_3$ (24, 25).

Another objective of the present investigation is the study of the V_K center in $RbMgF_3$. Shafer and McGuire (26) reported a hexagonal structure for $RbMgF_3$ similar to $BaTiO_3$. An x-ray Laue photograph with the beam incident along the c-axis shows that the $RbMgF_3$ samples used in this study have hexagonal symmetry. Figure 2 illustrates the $RbMgF_3$ crystal structure showing the basal plane with twelve F^- ions and seven Rb^+ ions in the first layer, and three Mg^{2+} ions in the second layer. The fluorine ions are arranged in equilateral triangle configurations in the c-axis plane. Any 2 of the 3 fluorine ions forming a triangle are possible lattice sites for the formation of a V_K center. Koumvakalis (27) has made a detailed optical investigation of the V_K center in $RbMgF_3$. Using polarized light, he showed that the V_K center molecular ions lie in the basal plane. He also identified the optical absorption bands arising from F, F_2 and F_3 centers in $RbMgF_3$ and showed that a

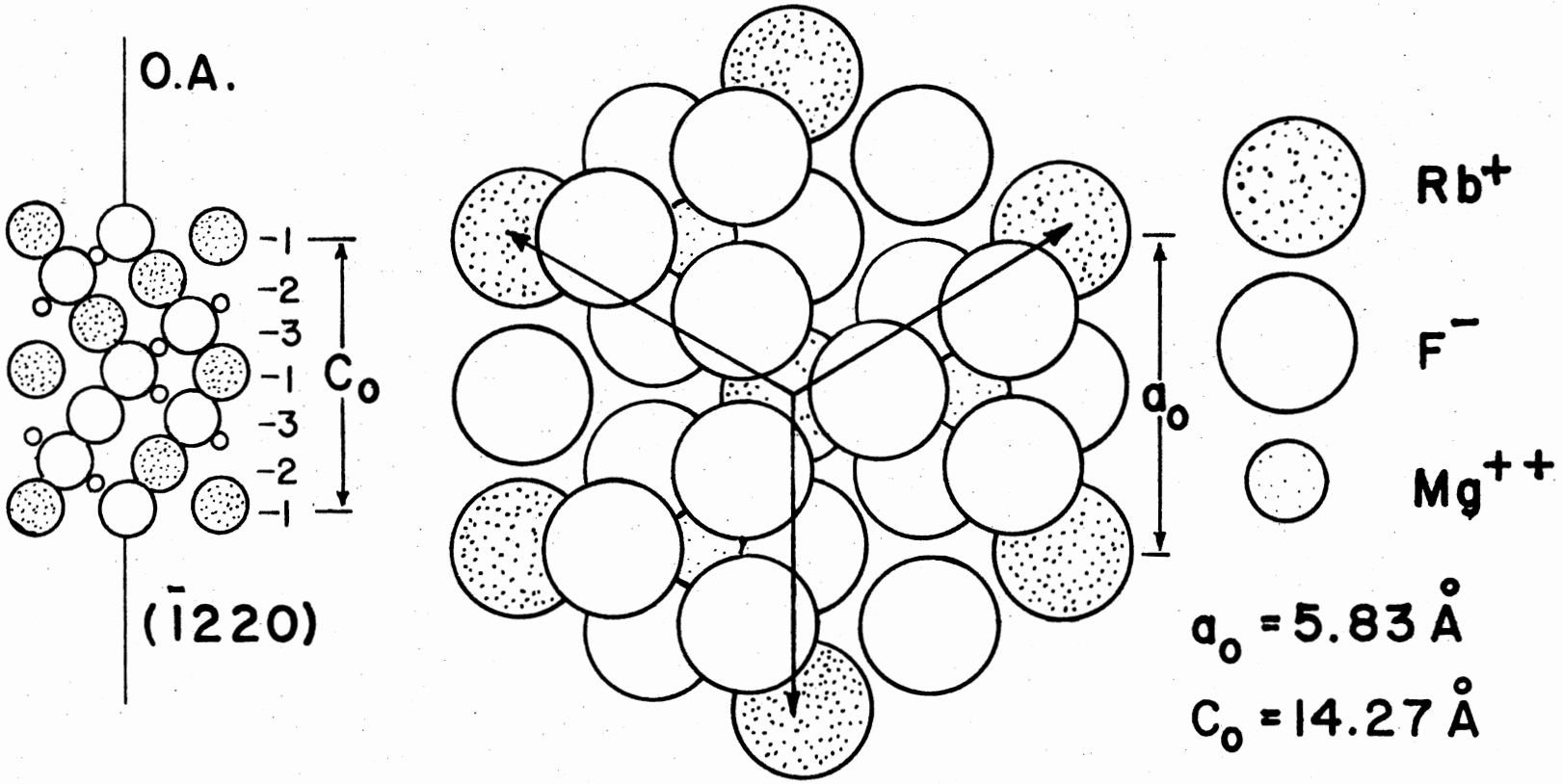

Figure 2. Crystal Structure of $RbMgF_3$

photochemical damage process is operative in the production of F centers in $KMgF_3$.

Results of the Present Work

Results of the investigation of the F center in $KMgF_3$ by the ENDOR technique are reported in this dissertation. Hyperfine interaction constants of the first and second shells of fluorine nuclei and of the first shell potassium nuclei have been determined. Origin of the 50 gauss linewidth for the F center ESR line has been explained by the measured values of the hyperfine constants for the nearest neighbour potassium and fluorine nuclei.

A complete characterization of the V_K center in $RbMgF_3$ is also reported here. Orientation of the V_K center with respect to the crystal axes is described. The decay temperature, principal values for the g factor, hyperfine interaction parameters, and a bent bond angle have all been measured.

CHAPTER II

GENERAL THEORY OF ENDOR

ENDOR Phenomenon

In an applied magnetic field, an $S = \frac{1}{2}$ spin system can have only two energy states, $M_s = \pm \frac{1}{2}$. The lower energy state $M_s = -\frac{1}{2}$ has a higher population than the upper energy state $M_s = +\frac{1}{2}$. The difference in energy between the two spin states is directly proportional to the applied static magnetic field. When the static magnetic field is so adjusted that the energy difference between the two states becomes equal to the energy of incident microwave photons an absorption of microwave energy will take place giving rise to an ESR signal.

When the electron spin is coupled to a nearby nuclear spin, a change in direction of the nuclear spin causes a change in the energy of the electron coupled to it. ENDOR is a double resonance technique in which the effect of a resonant change in the nuclear spin direction is observed via its effect on the ESR signal intensity.

Suppose we have a paramagnetic center $S = \frac{1}{2}$ coupled to a magnetic nucleus of spin $I = \frac{1}{2}$. In an externally applied magnetic field the energy levels of this system are as shown in Figure 3(a). Microwave photons induce electronic transitions ($\Delta M_s = \pm 1$, $\Delta M_I = 0$) giving rise to two ESR lines as indicated in Figure 3(a).

The energy difference between levels 1 and 4 or between 2 and 3 is about three orders of magnitude greater than that between 1 and 2 or

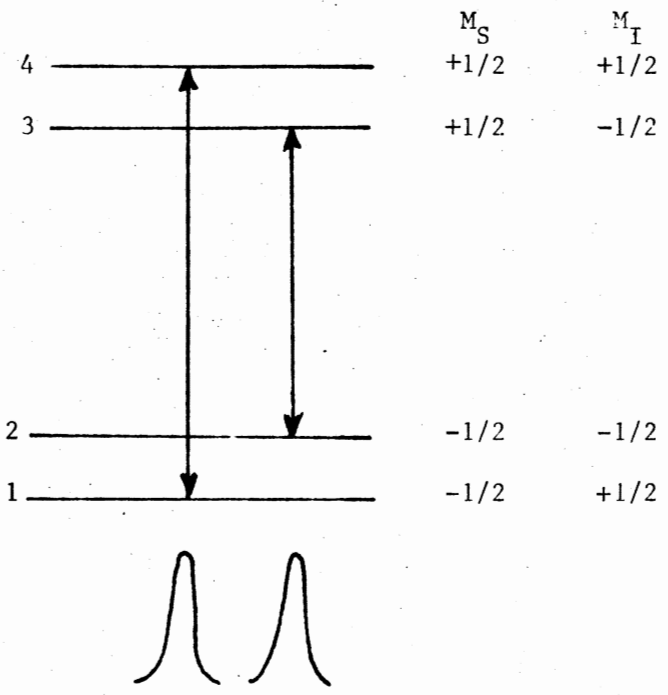

(a)

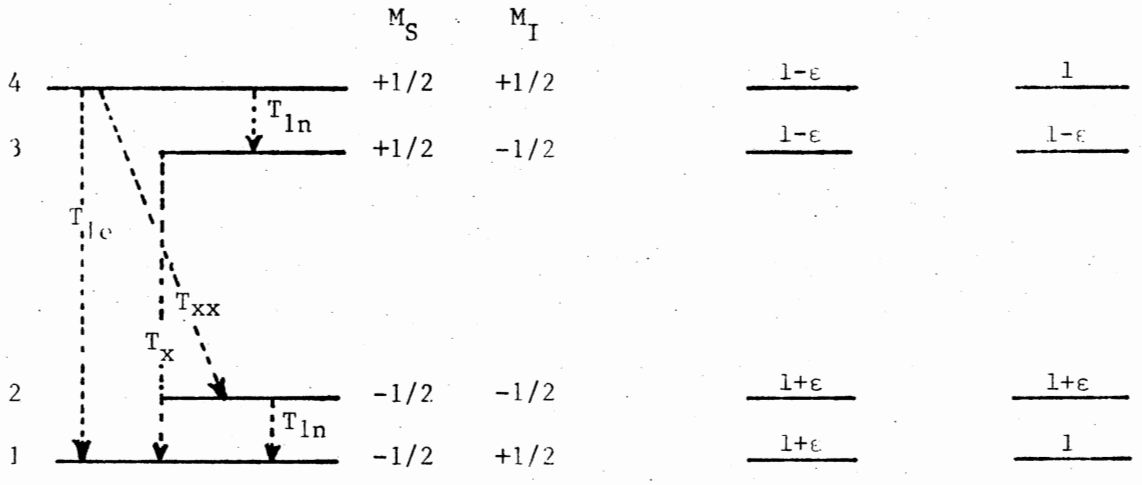

(b)

Figure 3. Energy Levels and Populations for the Discussion of ENDOR in an S = 1/2, I = 1/2 System

between 3 and 4. The difference of spin populations between two adjacent levels 3 and 4, for example, is quite small compared to the population difference between levels 2 and 3. A significant population difference between levels 3 and 4 can be created by saturating the electronic transition between levels 2 and 3. Under such a condition, a nuclear transition between levels 3 and 4, induced by incident rf radiation will give rise to an ENDOR line. A similar nuclear transition between the lower two hyperfine levels (1 and 2) will give rise to a second line.

These ENDOR frequencies can be obtained from a spin Hamiltonian. To first order, the spin Hamiltonian can be written as

$$H = g\beta\, S_Z H + AI_Z\, S_Z - g_n\, \beta_n\, HI_Z \,.$$

In an ENDOR transition the first term has no effect, hence an effective ENDOR Hamiltonian can be written as

$$H = AI_Z\, S_Z - g_n\, \beta_n\, HI_Z \,.$$

The energies for levels ($M_s = + \frac{1}{2}$, $M_I = - \frac{1}{2}$) and ($M_s = + \frac{1}{2}$, $M_I = + \frac{1}{2}$) (labelled 3 and 4 in Figure 3(a) are given by

$$- A/4 + \tfrac{1}{2}\, g_n\, \beta_n\, H$$

and

$$A/4 - \tfrac{1}{2}\, g_n\, \beta_n\, H \,.$$

An ENDOR transition between levels 3 and 4 gives a frequency

$$h\nu_1 = |A/2 - g_n \beta_n H| .$$

Similarly the energies for levels ($M_S = -\frac{1}{2}$, $M_I = +\frac{1}{2}$) and ($M_S = -\frac{1}{2}$, $M_I = -\frac{1}{2}$) (labelled 1 and 2 in Figure 3(a) are given by

$$-A/4 - \frac{1}{2} g_n \beta_n H$$

and

$$A/4 + \frac{1}{2} g_n \beta_n H .$$

An ENDOR transition between levels 1 and 2 gives a second frequency

$$h\nu_2 = |A/2 + g_n \beta_n H| .$$

From these two ENDOR frequencies the hyperfine constant A and the nuclear g factor g_n can be determined.

In the preceding example it was indicated that the hyperfine interaction was resolved in the ESR spectrum. However, often times ESR lines are inhomogeneously broadened--each such broad line is an envelope of a large number of very closely spaced lines. This is because each energy level is split into a large number of levels as a result of interaction of the paramagnetic center with magnetic nuclei of the lattice. In ENDOR a change in ESR signal intensity can be observed by driving a nuclear transition between two closely spaced energy levels, even though these two energy levels may not be resolved in the ESR spectrum.

Relaxation Paths and ENDOR Lines

As before consider an $S = \frac{1}{2}$ and $I = \frac{1}{2}$ spin system. On the left

side in Figure 3(b) T_{1e} and T_{1n} are the electron spin lattice and nuclear spin lattice relaxation times respectively. T_x and T_{xx} are the cross relaxation times. The middle portion of Figure 3(b) shows the populations of the different levels where $\varepsilon = g\beta H/KT$. The quantity $\varepsilon_n = g_n \beta_n H/KT$ is neglected. In general one finds that $T_{1e} < T_{1x} < T_{1n}$ (28). Suppose an electronic transition 1-4 is induced and the microwave power is increased to equalize the populations of levels 1 and 4. These new populations are shown on the right in Figure 3(b). The system is now irradiated with rf power and the rf frequency is swept while continuing to saturate the ESR transition. When the radio frequency matches the separation of levels 3 and 4, an induced emission from 4 to 3 will occur thus decreasing the population of level 4 and creating more room for ESR absorption from 1 to 4. An increase in the magnitude of the ESR signal will be observed. This is an ENDOR signal.

In the preceding paragraph saturation of microwave transition 1-4 was assumed. Now suppose the electronic transition 2-3 is saturated. On continuing the rf sweep, when the rf frequency matches the separation of levels 1 and 2, a second absorption of rf energy will take place and the spin population of level 2 will increase. Pumping more spins into level 2 by this rf absorption restores a population difference and there is again an enhancement of ESR absorption. This gives the second ENDOR signal.

This gives a simplified picture of ENDOR. In reality this phenomenon involves different relaxation paths, each with different relaxation times, by which the spin system attempts to restore an equilibrium population distribution among the different energy levels. (Some of these paths are shown on the left side in Figure 3(b)). The dynamics of these

relaxation processes is very involved.

Rf Enhancement Factor

Normally, the strength of the ENDOR signal depends upon the intensity of the rf magnetic field. However increased rf power may cause undesirable heating effects in the cavity. In many problems, strong ENDOR signals are obtained without any amplification of the incident rf power. This is explained by what is known as the rf enhancement factor.

In an ENDOR experiment, the rf magnetic field h_r and the applied static magnetic field H_o are perpendicular to each other.

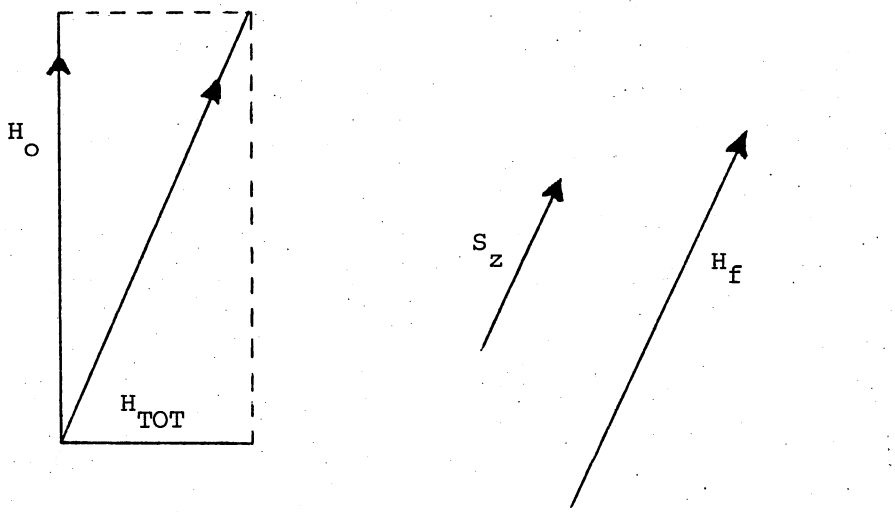

Figure 4. Enhancement of rf Magnetic Field h_1, by Hyperfine Field H_f

In the absence of an rf magnetic field, the electron spin is aligned along H_o. When the rf field is turned on the electron precesses about H_T. The direction of H_T changes as a result of change of the direction of h_r. This gives another slow precessional motion to the electron around H_o. H_f, the hyperfine field also keeps in steps with the electronic spin. This motion gives a component of H_f in the direction of h_r thereby producing an effective rf field of $h_r H_f/H_o$. The nucleus, unable to follow the rapid motion of the electron, sees an effective field of $h_r H_f/H_o$. In many cases the factor H_f/H_o is quite large, producing an effective field much greater than h_r. As a result of this increased field, an enhanced nuclear transition and hence an increased ENDOR signal is observed.

It can be shown that $H_f = - A M_s/g_n \beta_n$. For the F center ENDOR spectra in $KMgF_3$ it was observed that the ENDOR lines due to ^{39}K grow faster than the ENDOR lines due to ^{19}F. This is because the effective field is about one and a half times larger at a ^{39}K nucleus than the field at a ^{19}F nucleus.

CHAPTER III

EXPERIMENTAL PROCEDURE

Sample Preparation

The $KMgF_3$ and $RbMgF_3$ crystals used in this study were grown in the Crystal Growth Laboratory of Oklahoma State University by a modified Bridgman and Stockbarger method (29, 30, 31). In essence the method consists of the following. The starting materials, potassium fluoride (or rubidium fluoride) and magnesium fluoride are placed in a crucible at the end of an aluminum tube which is connected to a vacuum pump and to an argon gas tank so as to create an inert gas atmosphere over the melt or to flush the system with inert gas when necessary. The crucible with the Al_2O_3 tube is surrounded by a movable cylindrical shaped electric furnace with three sections of windings (6 turns per inch, 3 turns per inch, and 2 turns per inch). Details of furnace construction are given in the dissertations of C. T. Butler (32) and M. W. Wolf (33). The configuration provides a temperature gradient which can be moved relative to the starting materials contained in the crucible. The temperature gradient is moved by slowly raising the furnace, thereby lowering the temperature from a value slightly above the melting point to a value slightly below it. The crystallization starts at the lower portion of the melting region and moves slowly upward as the furnace is raised.

Smaller crystal samples were cut from the larger boules with a

diamond saw. A $KMgF_3$ sample was cleaved along a (100) plane and all the ENDOR data reported in this dissertation was obtained from this crystal. A Laue pattern was taken to verify the identity of the cleavage plane in this sample. The size of the sample was dimensioned 3.7 mm x 3.8 mm x 9 mm by using a diamond saw.

Single crystals of $RbMgF_3$ are difficult to cleave. Several samples were cut from a large boule and the orientations of the c-axis in them were determined using a polarizing microscope. A sample of 1.2 mm x 3.4 mm x 2.7 mm dimensions, with the optic axis perpendicular to the broad face was used in this study.

Defect Production

The F center in $KMgF_3$ is known to be stable at room temperature (19, 21). Thus, irradiation with 1.5 Mev electrons was carried out at room temperature. The $KMgF_3$ sample was wrapped in a piece of aluminum foil which was then taped to a heavy metal block. This assembly was then placed in front of the output window of a Van de Graaff accelerator at a distance of about 2 cm from it. The heavy metal block acts as a heat sink. The beam current was maintained at about 10 μA. To ensure that the sample was always at or near room temperature, the irradiation was done intermittently; the beam was turned on for 5 minutes followed by an off period of equal interval, and a steady stream of cool air was blown across the sample during irradiation.

The irradiation of $RbMgF_3$ for the production of V_K centers was carried out at liquid nitrogen temperature. The sample was placed in a styrofoam cup containing liquid nitrogen and the cup was covered with an insulating lid so that the sample was not exposed to light. This

cup was then placed in front of the output window of a Van de Graaff accelerator at a distance of 10 cm from it. An additional aluminum shield was placed between the cup and the accelerator window as a precaution against accidental ignition of the ozone built up in the liquid nitrogen. The irradiation period lasted for approximately three minutes. The sample was then kept in liquid nitrogen and never allowed to warm up throughout the entire ESR investigation.

ESR Spectrometer

Microwave Bridge

The microwave system is an X-band homodyne microwave bridge with a bias and a sample arm (Figure 5). The sample arm contains a precision attenuator to regulate the microwave power incident on the sample and thereby control the degree of saturation of the ESR transition. The klystron is locked to the resonant frequency of the sample cavity by means of a reflector-modulation stabilizer operating at a modulation frequency of 70 kilohertz. A low noise Schottky barrier diode acts as a microwave detector. The bias arm contains a phase shifter and an attenuator to regulate the detector bias. The bridge has a ferrite circulator to prevent unnecessary loss of signal.

Modulation and Detection System

For the study of F centers in $KMgF_3$, the static magnetic field was amplitude modulated at 4 kHz with the modulation coils attached to the poles of the magnet. For V_K centers in $RbMgF_3$, the amplitude modulation frequency was 100 kHz and the modulation coils were mounted on the cav-

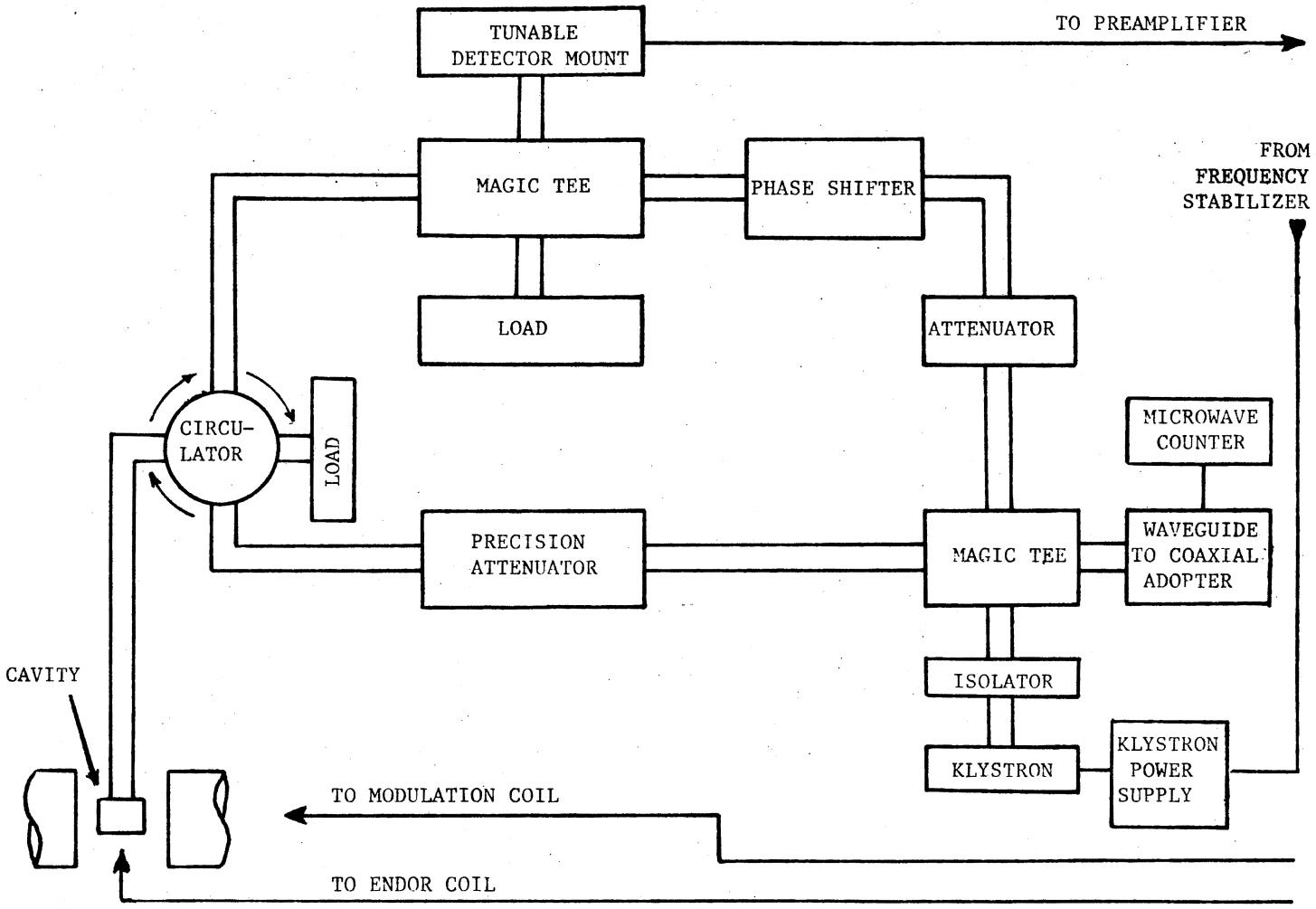

Figure 5. ESR Spectrometer

ity. A properly biased Schottky diode detects the microwave signal. This detected signal is amplified by a narrow band amplifier. The amplified signal is then fed into a phase sensitive detector, the reference signal for which is obtained from the same oscillator as used to amplitude modulate the static magnetic field. The output of the phase sensitive detector is used to drive a T-Y recorder.

Figure 6 illustrates the operations described above. Figure 6(a) shows the output of the microwave detector as a function of static magnetic field when the static magnetic field is not modulated. Figure 6(b) shows the variation of magnetic field with time when the modulation field is superimposed on the linearly varying static field. As a result of static magnetic field modulation, the output of the microwave detector contains a component at the modulation frequency having an amplitude which varies with magnetic field. This is schematically illustrated in Figure 6(c). Figure 6(d) schematically illustrates the output from the narrow-band amplifier as a function of static magnetic field when one passes through the ESR line. Figure 6(e) shows the output from the phase sensitive detector to be a derivative shape of the original absorption ESR line.

For the study of V_K centers in $RbMgF_3$, the sample after irradiation at liquid nitrogen temperature was loaded in the sample holder shown in Figure 7. The upper part of the sample holder is made of stainless steel tubing while the lower part is teflon with a flat platform at the end on which the sample sits. A spring loaded central rod made of lucite holds the sample firmly in place on the platform. The loaded holder was then lowered into a 5 mm I.D. finger Dewar filled with liquid nitrogen. This arrangement was then placed in a Varian V-4531 rectangular cavity

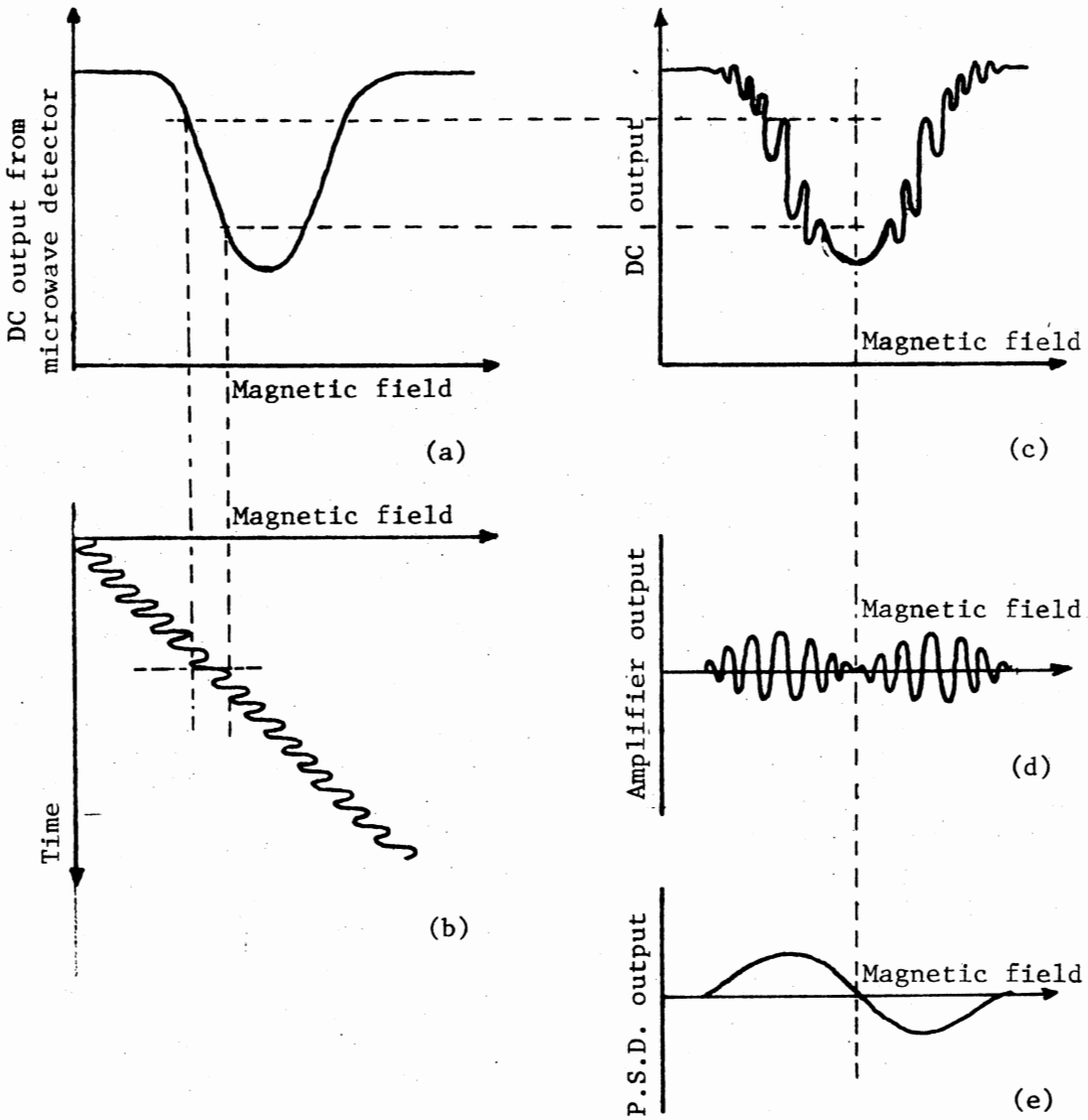

Figure 6. Waveforms Illustrating the Operation of a Modulation and Detection System

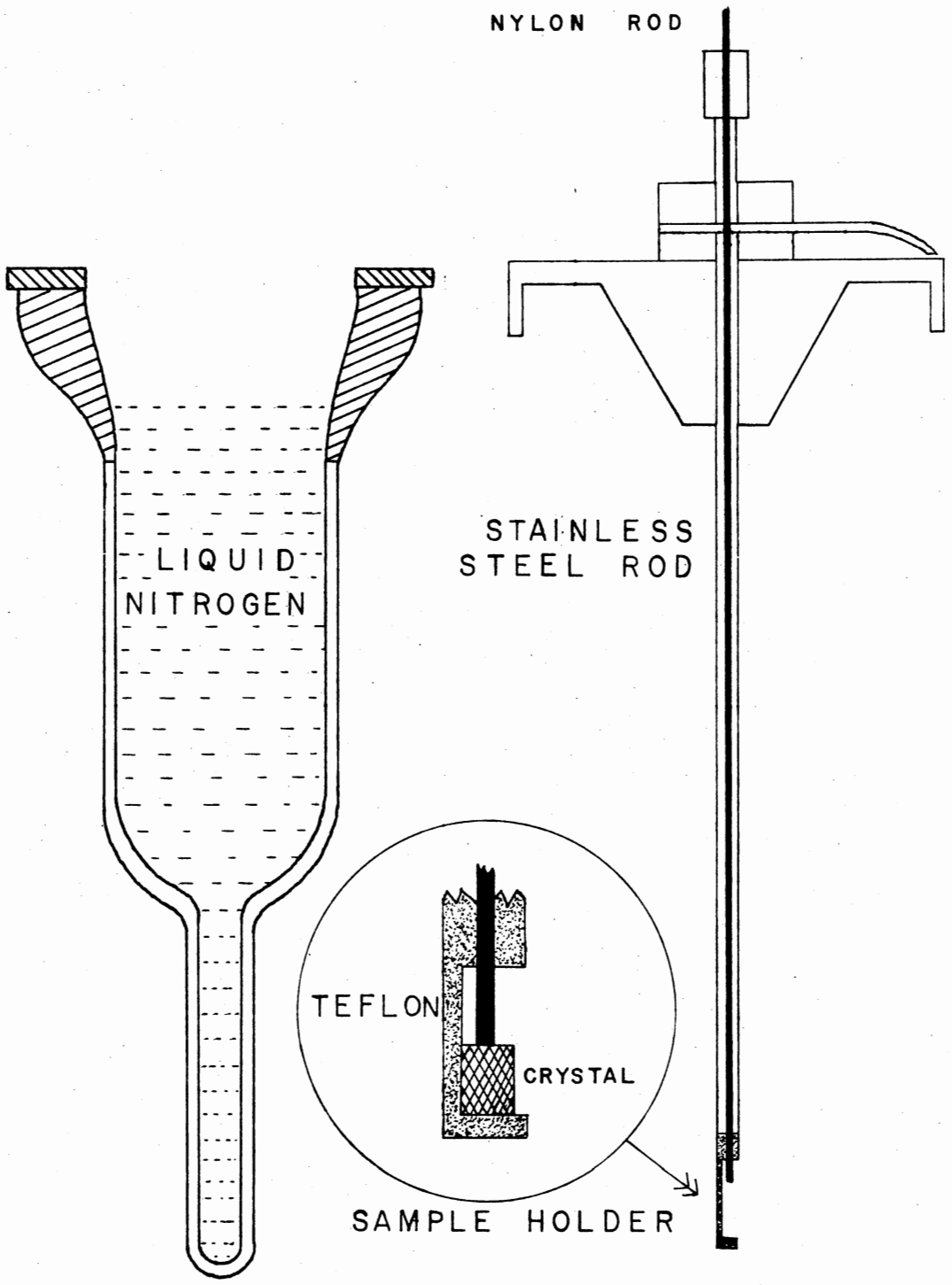

Figure 7. Sample Holder Used in ESR Measurements of V_K Centers in $KMgF_3$

for ESR measurements.

Magnet System

A 9 inch Varian V-7200 electromagnet was used in the ENDOR study of F centers in $KMgF_3$. It has 2 water-cooled, low-impedence (.5 ohm) coils connected in series. Two series connected thermal switches, one on each coil, protect the magnet from possible damage by temperatures above $70^{o}C$. The supply delivers field regulated dc power into a 1 ohm load and the magnetic field is indicated directly in gauss by the field set controls. In this field regulated supply, a Hall probe mounted on one of the pole caps, senses any variations in field intensity and supplies an error signal thereby adjusting the current. This arrangement gives a long term magnetic field stability of approximately 5 milligauss.

The magnet used for the V_K center study was a Varian 6 inch current-regulated electromagnet, Model 4007-1. A Varian V-4560 100 kHz modulation unit was used to modulate the static magnetic field.

ENDOR Spectrometer

ENDOR Cavity

The microwave cavity used in the present ENDOR study operates in the cylindrical TE_{011} mode. A rectangular cavity was found to be less satisfactory because of difficulties encountered in finding a suitable ENDOR coil configuration. The present cylindrical cavity has a loaded Q of about 10,000 at liquid nitrogen temperature.

Figure 8 shows a cross sectional view of the cavity with the sample in place. A three-turn rf coil of 27 gauge wire was wound directly on

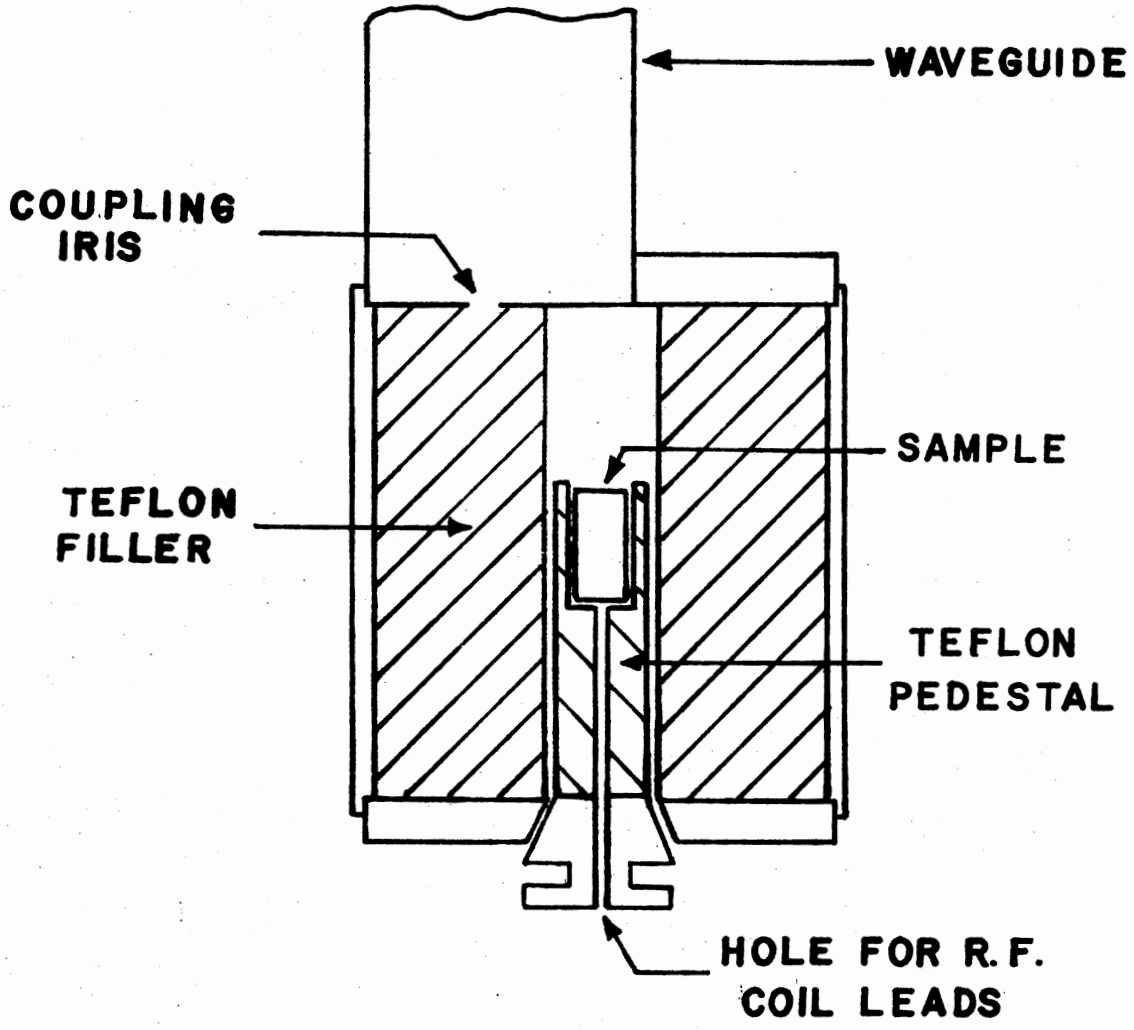

Figure 8. Cross-sectional View of the ENDOR Cavity With Sample in Place

the sample and the leads were taken out of the cavity through a hole bored along the axis of the cylindrical teflon pedestal. The hole was sealed off with Dow Corning silicone grease so as to maintain vacuum in the waveguide and thus prevent liquid nitrogen from entering the cavity.

It was found that the cavity Q was very sensitive to the exact positioning of the ENDOR coil in the cavity. The wire-leads acted as a transmission line and allowed microwave energy to escape from the cavity, thereby deteriorating the cavity Q. Nevertheless after several attempts a good cavity Q could be obtained.

RF System and Signal Averager

The rf system illustrated in Figure 9 consists of an attenuator, a preamplifier, an HP model 8601A sweep generator (.1 MHz to 110 MHz), and an rf broad band power amplifier. (For simplicity, the block diagram in Figure 9 does not show the attenuator or preamplifier.) The signal averager, a dedicated minicomputer made by Nicolet Instrument Corporation (1070 series computer), has 2K words of memory grouped into 4 quarters. The signal averager puts out a saw tooth (ramp) voltage waveform of 4 volts maximum amplitude thus providing a voltage proportional to memory address. The time period of this voltage wave form is controlled by the signal averager's dwell time setting while the amplitude is controlled by the external attenuator setting. The saw tooth waveform from the signal averager is used to externally FM modulate the sweep generator, and the resulting rf sweep width is controlled by adjusting the amplitude of the ramp voltage with the external attenuator.

The sweep generator puts out a range of rf frequencies which when incident on the sample can drive nuclear transitions. If one of the

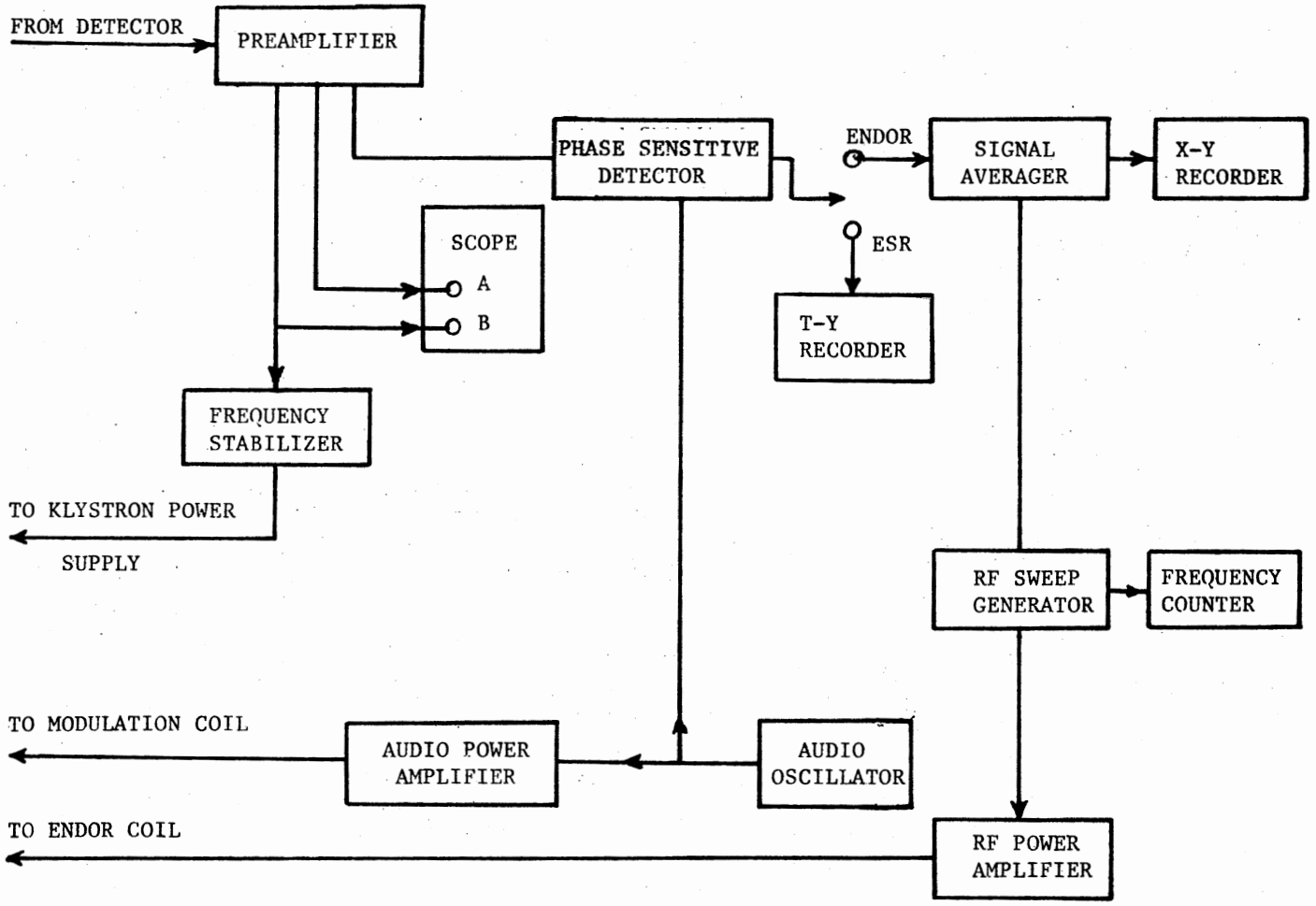

Figure 9. ENDOR Spectrometer

possible nuclear transitions is driven, an increase in the signal level detected by the phase sensitive detector in the ESR system is observed. This changing ESR signal is fed into the signal averager, then converted to a digital signal and finally stored in the memory. A large number of scans over the same rf frequency range causes the ENDOR signal to increase relative to the noise. The signal grows as N while the random noise grows as $\sqrt{N}$, where N is the number of sweeps. A large number of sweeps was usually needed for the ENDOR signal to be observable.

CHAPTER IV

THEORETICAL ANALYSIS OF MAGNETIC RESONANCE SPECTRA

The general spin Hamiltonian for an F center is given by

$$H = \beta \cdot \vec{H} \cdot \overleftrightarrow{g} \cdot \vec{S} + \sum_{\alpha} \left[\vec{I}_{\alpha} \cdot \overleftrightarrow{A}_{\alpha} \cdot \vec{S} + \vec{I}_{\alpha} \cdot \overleftrightarrow{Q}_{\alpha} \cdot \vec{I}_{\alpha} - g_n \beta_n \vec{H} \cdot \vec{I}_{\alpha} \right] \tag{1}$$

where the summation in over all neighbouring nuclei, as the electron usually interacts with many nuclei. The first and last terms are the electron Zeeman and nuclear Zeeman interactions. The second and third terms represent the hyperfine interactions and quadrupole interactions, respectively.

The hyperfine interaction tensor $\overleftrightarrow{A}$ may be divided into two parts--an isotropic part and an anisotropic part with zero trace.

$$\overleftrightarrow{A} = a + \overleftrightarrow{B}$$

$$\sum_{i} B_{ii} = 0$$

The isotropic or Fermi interaction term is proportional to the density of the unpaired electron at the interacting nucleus and is given by

$$a = (8/3)\, \pi\, g\, \beta\, g_n \beta_n \left| \psi(\vec{r}_i) \right|^2 .$$

$\left| \psi(\vec{r}_i) \right|^2$ in the probability density of the unpaired electron evaluated at the nuclear position $\vec{r}_i$. The tensor $\overleftrightarrow{B}$ represents the anisotropic part of the hyperfine interaction. This anisotropic part describes the

dipole-dipole interaction of the distributed electronic magnetic moment with the nuclear magnetic moment. The elements of this tensor are given by

$$B_{ik} = g \beta g_n \beta_n \int [3 x_i x_k / r^5 - (\delta_{ik} | r^3)] |\psi(r)|^2 \, dv$$

where x_i and x_k are the cartesian coordinates of the magnetic nucleus with respect to the distributed electronic dipole.

The quadrupole term in the spin Hamiltonian results from the interaction of a nuclear quadrupole moment with the crystalline electric field gradient at the nuclear site. When observable, this effect provides information about the lattice distortion surrounding the defect. For a nucleus with I = 1/2, such as fluorine in the present case, the quadrupole moment is zero and hence the quadrupole interaction term does not exist. In the case of potassium (I = 3/2) nuclei, a quadrupole interaction is possible but none was observed in the present investigation.

The effective ENDOR Hamiltonian describing the interaction between the unpaired electron and a single nucleus can be written as

$$H = g\beta \vec{H} \cdot \vec{S} + \vec{I} \cdot \overleftrightarrow{A} \cdot \vec{S} - g_n \beta_n \vec{H} \cdot \vec{I}$$

In some cases, nuclei in the same shell interact with each other. An extra term has to be included in the Hamiltonian to describe this interaction. The coordinate systems defined below are suitable for use in converting the Hamiltonian to a form suitable for programming on a digital computer.

x,y,z : Magnetic field coordinate system so chosen that the z direction is along the magnetic field.

x_c, y_c, z_c: Crystal coordinate system.

x_1, y_1, z_1: Principal axis system for the hyperfine tensor $\overleftrightarrow{A}$.

Rewriting the effective ENDOR Hamiltonian in terms of the coordinate systems gives

$$H = g\beta H S_z + I_{x_1} A_x S_{x_1} + I_{y_1} A_y S_{y_1} + I_{z_1} A_z S_{z_1} - g_n \beta_n H I_z .$$

To write the Hamiltonian in only one coordinate system, the magnetic field coordinate system, the following transformation matrices are used.

[T]: Transforms principal axis system of the $\overleftrightarrow{A}$ tensor to the crystal coordinate system.

[R]: Transforms crystal coordinate system to the magnetic field coordinate system.

[TR] = [T][R]: Transforms principal axis system of $\overleftrightarrow{A}$ tensor to the magnetic field coordinate system.

The components of $\vec{I}$ and $\vec{S}$ in the $\overleftrightarrow{A}$ tensor's principal axis coordinate system can be expressed in the magnetic field coordinate system by the following relations.

$$\begin{pmatrix} I_{x_1} \\ I_{y_1} \\ I_{z_1} \end{pmatrix} = [TR] \begin{pmatrix} I_x \\ I_y \\ I_z \end{pmatrix}$$

and

$$\begin{pmatrix} S_{x_1} \\ S_{y_1} \\ S_{z_1} \end{pmatrix} = [TR] \begin{pmatrix} S_x \\ S_y \\ S_z \end{pmatrix}$$

Using the above transformations, the Hamiltonian can be written as

$$
\begin{aligned}
H = {} & g\beta H S_z - g_n\beta_n H I_z \\
& + A_x [TR(1,1)\ TR(1,1)\ I_x S_x + TR(1,2)\ TR(1,1)\ I_y S_x \\
& \quad + TR(1,3)\ TR(1,1)\ I_z S_x + TR(1,1)\ TR(1,2)\ I_x S_y \\
& \quad + TR(1,2)\ TR(1,2)\ I_y S_y + TR(1,3)\ TR(1,2)\ I_z S_y \\
& \quad + TR(1,1)\ TR(1,3)\ I_x S_z + TR(1,2)\ TR(1,3)\ I_y S_z \\
& \quad + TR(1,3)\ TR(1,3)\ I_z S_z] \\
& + A_y [TR(2,1)\ TR(2,1)\ I_x S_x + TR(2,2)\ TR(2,1)\ I_y S_x \\
& \quad + TR(2,3)\ TR(2,1)\ I_z S_x + TR(2,1)\ TR(2,2)\ I_x S_y \\
& \quad + TR(2,2)\ TR(2,2)\ I_y S_y + TR(2,3)\ TR(2,2)\ I_z S_y \\
& \quad + TR(2,1)\ TR(2,3)\ I_x S_z + TR(2,2)\ TR(2,3)\ I_y S_z \\
& \quad + TR(2,3)\ TR(2,3)\ I_z S_z] \\
& + A_z [TR(3,1)\ TR(3,1)\ I_x S_x + TR(3,2)\ TR(3,1)\ I_y S_x \\
& \quad + TR(3,3)\ TR(3,1)\ I_z S_x + TR(3,1)\ TR(3,2)\ I_x S_y \\
& \quad + TR(3,2)\ TR(3,2)\ I_y S_y + TR(3,3)\ TR(3,2)\ I_z S_y
\end{aligned}
$$

$$+ TR(3,1)\ TR(3,3)\ I_x S_z + TR(3,2)\ TR(3,3)\ I_y S_z$$

$$+ TR(3,3)\ TR(3,3)\ I_z S_z] .$$

In order to simplify the appearance of the Hamiltonian a new set of parameters is introduced. The effective ENDOR Hamiltonian now becomes

$$H = g\beta H S_z - g_n\beta_n H I_z$$

$$+ W1\ I_x S_x + W2\ I_y S_x + W3\ I_z S_x$$

$$+ W2\ I_x S_y + W4\ I_y S_y + W5\ I_z S_y$$

$$+ W3\ I_x S_z + W5\ I_y S_z + W6\ I_z S_z$$

where

$$W1 = A_x\ TR(1,1)\ TR(1,1) + A_y\ TR(2,1)\ TR(2,1) + A_z\ TR(3,1)\ TR(3,1),$$

$$W2 = A_x\ TR(1,2)\ TR(1,1) + A_y\ TR(2,2)\ TR(2,1) + A_z\ TR(3,2)\ TR(3,1),$$

$$W3 = A_x\ TR(1,3)\ TR(1,1) + A_y\ TR(2,3)\ TR(2,1) + A_z\ TR(3,3)\ TR(3,1),$$

$$W4 = A_x\ TR(1,2)\ TR(1,2) + A_y\ TR(2,2)\ TR(2,2) + A_z\ TR(3,2)\ TR(3,2),$$

$$W5 = A_x\ TR(1,3)\ TR(1,2) + A_y\ TR(2,3)\ TR(2,2) + A_z\ TR(3,3)\ TR(3,2),$$

and

$$W6 = A_x\ TR(1,3)\ TR(1,3) + A_y\ TR(2,3)\ TR(2,3) + A_z\ TR(3,3)\ TR(3,3).$$

By introducing the raising and lowering operators

$$S_+ = S_x + i\, S_y$$

$$S_- = S_x - i\, S_y$$

$$I_+ = I_x + i\, I_y$$

$$I_- = I_x - i\, I_y$$

the Hamiltonian in the magnetic field coordinate system can be written as

$$\begin{aligned} H = {} & g\beta H S_z - g_n\beta_n H I_z + W6\, I_z S_z \\ & + 1/4(W1 - W4 - 2iW2)\, I_+ S_+ \\ & + 1/4(W1 + W4)\, I_- S_+ \\ & + 1/4(W1 + W4)\, I_+ S_- \\ & + 1/4(W1 - W4 + 2iW2)\, I_- S_- \\ & + 1/2(W3 - iW5)\, I_z S_+ \\ & + 1/2(W3 + iW5)\, I_z S_- \\ & + 1/2(W3 - iW5)\, I_+ S_z \\ & + 1/2(W3 + iW5)\, I_- S_z \,. \end{aligned}$$

Defining the following parameters

$$Q1 = 1/4(W1 - W4 + 2iW2)$$

$$Q2 = 1/4(W1 + W4)$$

$$Q3 = 1/2(W3 + iW5),$$

the Hamiltonian becomes

$$H = g\beta H S_z + W6 I_z S_z - g_n\beta_n H I_z$$

$$+ Q1^* I_+ S_+ + Q2 I_- S_+ + Q2 I_+ S_- + Q1 I_- S_-$$

$$+ Q3^* I_z S_+ + Q3 I_z S_- + Q3^* I_+ S_z + Q3 I_- S_z .$$

This last form of the effective ENDOR Hamiltonian will now be used to find the Hamiltonian matrix elements for the fluorine ENDOR. The ^{19}F nucleus has $I = 1/2$ and hence $|M_S = \pm \frac{1}{2}, M_I = \pm \frac{1}{2}\rangle$ is chosen as a basis set. This basis set has 4 vectors and thus allows the effective ENDOR Hamiltonian to be written in the form of a 4 x 4 matrix. The diagonalization of this matrix gives the relative energy levels. Since the Hamiltonian matrix is Hermitian only the lower half of the matrix elements are needed to find the eigenvalues.

Table II shows the lower half of the effective ENDOR Hamiltonian matrix for the case when $I = \frac{1}{2}$.

The matrix elements listed in Table II are given below.

$$A(1,1) = \tfrac{1}{2} g\beta H + \tfrac{1}{4} W6 - \tfrac{1}{2} g_n\beta_n H$$

$$A(2,2) = \tfrac{1}{2} g\beta H - \tfrac{1}{4} W6 + \tfrac{1}{2} g_n\beta_n H$$

$$A(3,3) = -\tfrac{1}{2} g\beta H + \tfrac{1}{4} W6 + \tfrac{1}{2} g_n\beta_n H$$

TABLE II

LOWER HALF OF THE HAMILTONIAN MATRIX ELEMENTS
FOR ^{19}F NUCLEI ENDOR

	$\|+\frac{1}{2}, +\frac{1}{2}\rangle$	$\|+\frac{1}{2}, -\frac{1}{2}\rangle$	$\|-\frac{1}{2}, -\frac{1}{2}\rangle$	$\|-\frac{1}{2}, +\frac{1}{2}\rangle$
$\|+\frac{1}{2}, +\frac{1}{2}\rangle$	A(1,1)			
$\|+\frac{1}{2}, -\frac{1}{2}\rangle$	A(2,1)	A(2,2)		
$\|-\frac{1}{2}, -\frac{1}{2}\rangle$	A(3,1)	A(3,2)	A(3,3)	
$\|-\frac{1}{2}, +\frac{1}{2}\rangle$	A(4,1)	A(4,2)	A(4,3)	A(4,4)

$$A(4,4) = -\tfrac{1}{2} g\beta H - \tfrac{1}{4} W6 - \tfrac{1}{2} g_n\beta_n H$$

$$A(2,1) = \tfrac{1}{2} Q3$$

$$A(3,1) = Q1$$

$$A(3,2) = -\tfrac{1}{2} Q3$$

$$A(4,1) = \tfrac{1}{2} Q3$$

$$A(4,2) = Q2$$

$$A(4,3) = -\tfrac{1}{2} Q3^*.$$

The effective Hamiltonian for the ^{39}K ENDOR has the same form as the one used for the ^{19}F ENDOR analysis, the only difference being that now one uses I = 3/2 instead of I = 1/2 when the Hamiltonian is converted over into a matrix form. The basis set appropriate for the ^{39}K case has 8 states. The energy eigenvalues of the system can be obtained by diagonalizing the Hamiltonian matrix. Since the Hamiltonian matrix is Hermitian, only matrix elements in the lower half of the triangle are needed, and are given in Table III.

The values of the matrix elements listed in Table III are as follows.

$$A(1,1) = 1/2\ g\beta H + 3/4\ W6 - 3/2\ g_n\beta_n H$$

$$A(2,2) = 1/2\ g\beta H + W6/4 - g_n\beta_n H/2$$

$$A(3,3) = 1/2\ g\beta H - W6/4 + g_n\beta_n H/2$$

TABLE III

LOWER HALF OF THE HAMILTONIAN MATRIX ELEMENTS FOR ^{39}K ENDOR

	$\left\|\frac{1}{2},3/2\right>$	$\left\|\frac{1}{2},\frac{1}{2}\right>$	$\left\|\frac{1}{2},-\frac{1}{2}\right>$	$\left\|\frac{1}{2},-3/2\right>$	$\left\|-\frac{1}{2},-3/2\right>$	$\left\|-\frac{1}{2},-\frac{1}{2}\right>$	$\left\|-\frac{1}{2},\frac{1}{2}\right>$	$\left\|-\frac{1}{2},3/2\right>$
$\left<\frac{1}{2},3/2\right\|$	A(1,1)							
$\left<\frac{1}{2},\frac{1}{2}\right\|$	A(2,1)	A(2,2)						
$\left<\frac{1}{2},-\frac{1}{2}\right\|$	0	A(3,2)	A(3,3)					
$\left<\frac{1}{2},-3/2\right\|$	0	0	A(4,3)	A(4,4)				
$\left<-\frac{1}{2},-3/2\right\|$	0	0	A(5,3)	A(5,4)	A(5,5)			
$\left<-\frac{1}{2},-\frac{1}{2}\right\|$	0	A(6,2)	A(6,3)	A(6,4)	A(6,5)	A(6,6)		
$\left<-\frac{1}{2},\frac{1}{2}\right\|$	A(7,1)	A(7,2)	A(7,3)	0	0	A(7,6)	A(7,7)	
$\left<-\frac{1}{2},3/2\right\|$	A(8,1)	A(8,2)	0	0	0	0	A(8,7)	A(8,8)

$$A(4,4) = 1/2\ g\beta H - 3/4\ W6 + 3/2\ g_n\beta_n H$$

$$A(5,5) = -1/2\ g\beta H + 3/4\ W6 + 3/2\ g_n\beta_n H$$

$$A(6,6) = -1/2\ g\beta H + W6/4 + g_n\beta_n H/2$$

$$A(7,7) = -1/2\ g\beta H - W6/4 - g_n\beta_n H/2$$

$$A(8,8) = -1/2\ g\beta H - 3/4\ W6 - 3/2\ g_n\beta_n H$$

$$A(2,1) = \frac{\sqrt{3}}{2}\ Q3$$

$$A(3,2) = Q3$$

$$A(4,3) = \frac{\sqrt{3}}{2}\ Q3$$

$$A(5,3) = \sqrt{3}\ Q1$$

$$A(5,4) = -\frac{3}{2}\ Q3$$

$$A(6,2) = 2\ Q1$$

$$A(6,3) = -Q3/2$$

$$A(6,4) = \sqrt{3}\ Q2$$

$$A(6,5) = -\frac{\sqrt{3}}{2}\ Q3^*$$

$$A(7,1) = \sqrt{3}\ Q1$$

$$A(7,2) = Q3/2$$

$$A(7,3) = 2\ Q2$$

$$A(7,6) = -\,Q3^*$$

$$A(8,1) = \frac{3}{2}\,Q3$$

$$A(8,2) = \sqrt{3}\,Q2$$

$$A(8,7) = -\,\frac{\sqrt{3}}{2}\,Q3^*$$

CHAPTER V

EXPERIMENTAL RESULTS

The ESR spectrum of the F center in $KMgF_3$, taken at liquid nitrogen temperature, is shown in Figure 10. It shows no dependence on magnetic field orientation and has a g value of 2.0011 ± .001. The ESR spectrum consists of 9 lines of unequal intensity, the central line is most intense while the intensity of lines decreases as one goes from the center to either side. The individual linewidth is about 50 gauss. The F center ESR spectrum can be power saturated fairly easily at liquid nitrogen temperature and, as a result, all of the ENDOR results presented in this chapter were obtained at liquid nitrogen temperature.

ENDOR Spectra of First Shell ^{39}K Nuclei

Figure 11 shows the ENDOR spectrum from the first shell potassium nuclei when the magnetic field is along a [100] direction. There are two pairs of lines attributed to ^{39}K, one pair being twice as intense as the other pair. The smaller, most widely split pair of lines in Figure 11 are assigned to the second shell fluorine nuclei and will be discussed later in this chapter. Experimentally measured values of ENDOR frequencies from the first shell ^{39}K nuclei are given in Table IV.

The 2:1 intensity ratio for the two pairs of ^{39}K ENDOR lines observed in Figure 11 can be understood from the following consideration. For a particular direction of applied magnetic field, specific nuclei

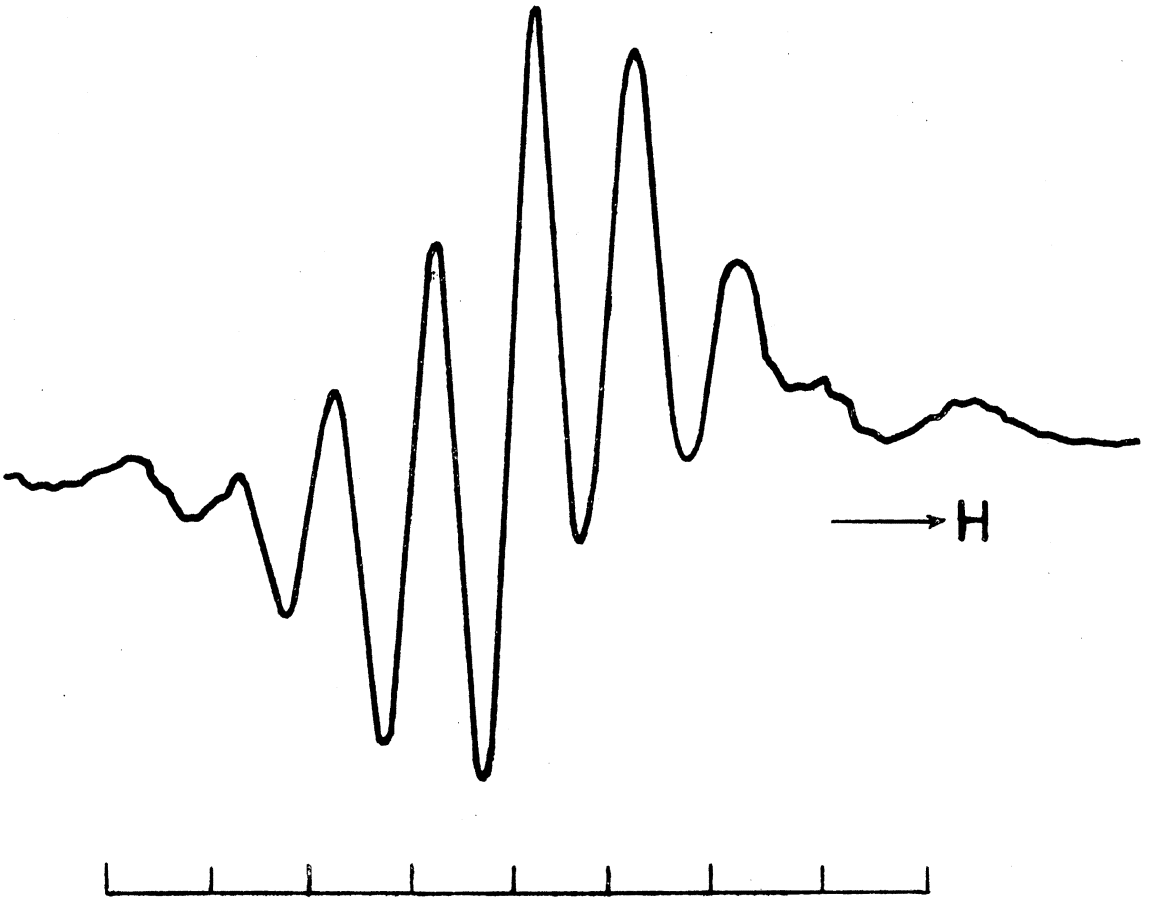

Figure 10. ESR Spectrum of F Centers in $KMgF_3$

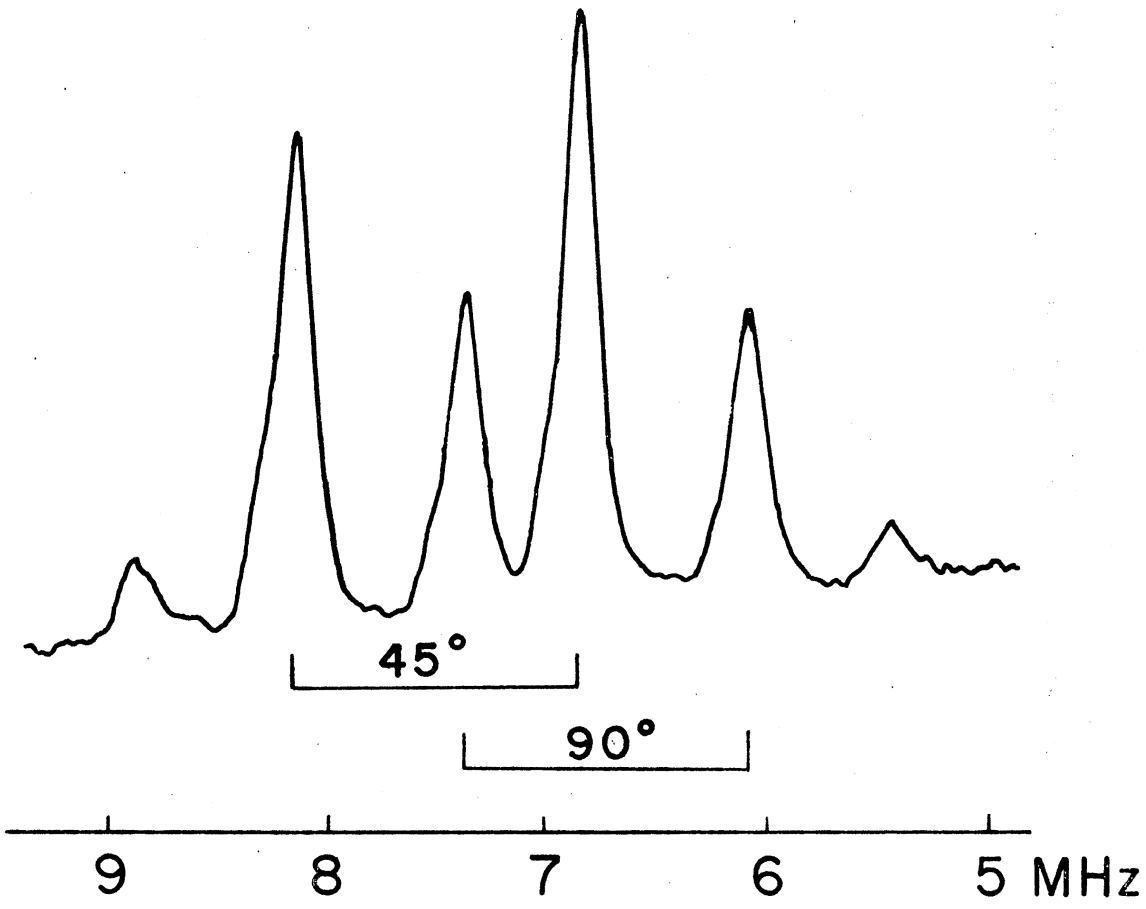

Figure 11. ENDOR Spectrum of ^{39}K Nuclei, H//[100]

TABLE IV

SUMMARY OF THE RESULTS OF ^{39}K NUCLEI ENDOR MEASUREMENTS

Direction of the Applied Mag. Field	Experimentally Determined ENDOR Freq. in MHz (± .01 MHz)	Calculated Value of ENDOR Freq. in MHz	Transition
[100]	8.169	8.155	$\|M_S = -1/2, M_I = -1/2\rangle \leftrightarrow \|M_S = -1/2, M_I = +1/2\rangle$
	6.882	6.871	$\|M_S = +1/2, M_I = -1/2\rangle \leftrightarrow \|M_S = +1/2, M_I = +1/2\rangle$
	7.389	7.395	$\|M_S = -1/2, M_I = -1/2\rangle \leftrightarrow \|M_S = -1/2, M_I = +1/2\rangle$
	6.096	6.105	$\|M_S = +1/2, M_I = -1/2\rangle \leftrightarrow \|M_S = +1/2, M_I = +1/2\rangle$
[110]	8.846	8.870	$\|M_S = -1/2, M_I = -1/2\rangle \leftrightarrow \|M_S = -1/2, M_I = +1/2\rangle$
	7.603	7.580	$\|M_S = +1/2, M_I = -1/2\rangle \leftrightarrow \|M_S = +1/2, M_I = +1/2\rangle$
	7.750	7.784	$\|M_S = -1/2, M_I = -1/2\rangle \leftrightarrow \|M_S = -1/2, M_I = +1/2\rangle$
	6.478	6.500	$\|M_S = +1/2, M_I = -1/2\rangle \leftrightarrow \|M_S = +1/2, M_I = +1/2\rangle$

within a shell will be distinguished by considering the angle between the magnetic field and the line from the nucleus to the center of the vacancy. For the magnetic field along the [100] direction, the first shell ^{39}K nuclei can be divided into two groups--one group makes an angle of 45^{o} with the F center while the other group makes an angle of 90^{o}. There are twice as many ^{39}K nuclei in the 45^{o} group as there are in the 90^{o} group. To convince oneself of this, the three distinguishable F center sites arising from the defect's axial symmetry must be considered.

The ^{39}K nucleus has I = 3/2 and hence the electronic spin-up state $M_S = + 1/2$ has four energy levels ($M_I = \pm 3/2, \pm 1/2$). ENDOR transitions ($\Delta M_I = \pm 1$) in the electronic spin-up state will give rise to three ENDOR lines in the general case. Since only one ENDOR frequency was observed from the ^{39}K electron spin-up set of levels, the nuclear quadrupole interaction must be negligible. This makes the four levels equally spaced in energy and gives a single line (three-fold degenerate), as observed. Similarly, nuclear transitions in the electronic spin-down states give only one observable ENDOR line. Hence, ^{39}K nuclei making a particular angle with the magnetic field give one pair of lines separated from each other by $2g_n\beta_n H$. So for the orientation of magnetic field along a [100] direction, the two observed pairs of lines are directly explained in terms of the crystal structure and the lack of a significant nuclear quadrupole interaction.

Figure 12 is a trace of the ^{39}K ENDOR spectrum for the magnetic field 15^{o} off the [100] direction in the (100) plane. It shows four pairs of lines. All the ^{39}K nuclei which made a 45^{o} angle with the magnetic field for the [100] orientation (this case has been discussed

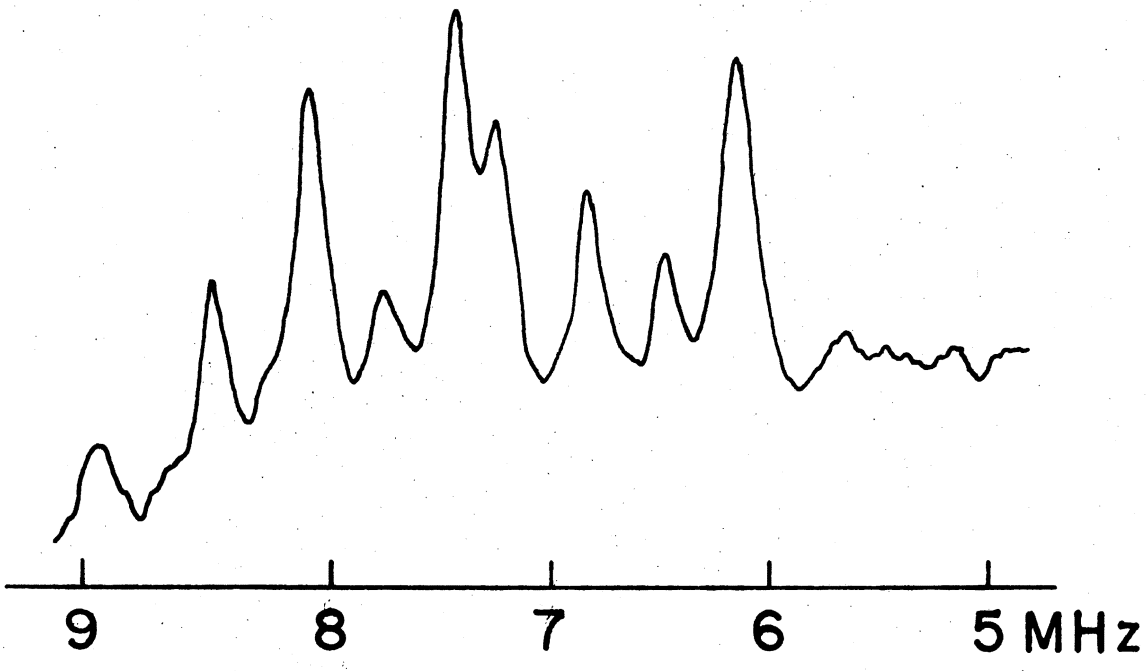

Figure 12. ENDOR Spectrum of ^{39}K Nuclei for Magnetic Field 15° off a [100] Direction

in the last paragraph) now break up into three inequivalent groups. Each group makes a different angle with the magnetic field, and thus gives rise to three pairs of lines. The fourth pair of lines in Figure 12 comes from those nuclei which made a 90° angle with the magnetic field in the [100] orientation.

Figure 13 shows the ENDOR spectrum for the first shell ^{39}K nuclei when the magnetic field is along the [110] direction. It consists of three pairs of lines. One pair of lines is assigned to potassium nuclei making a 0° angle with the magnetic field, the second pair is assigned to potassium nuclei making a 60° angle, and the third pair is assigned to potassium nuclei making a 90° angle. The low frequency line of the 0° pair and the high frequency line of the 60° pair are not well resolved, and this superimposition causes the second line in the spectrum to be bigger than the other lines. The measured values of the first shell ^{39}K transition frequencies for a [110] direction of the applied magnetic field are given in Table IV.

Calculation of Hyperfine Parameters for ^{39}K Nucleus

Of the ten observed ENDOR lines for high symmetry directions of the magnetic field (four for the [100] direction and six for the [110] direction), only eight are useful since the 90° pairs in each orientations are redundant. From the symmetry of the first shell potassium site, three parameters (A_x, A_y, and A_z) are needed to describe the hyperfine tensor. The directions of the principal axes are fixed. For an F center having a [100] symmetry axis, the principal axes of the first shell ^{39}K nuclei are directed along [100], [01$\bar{1}$], and [011] directions.

To obtain the three hyperfine interaction constants of the ^{39}K

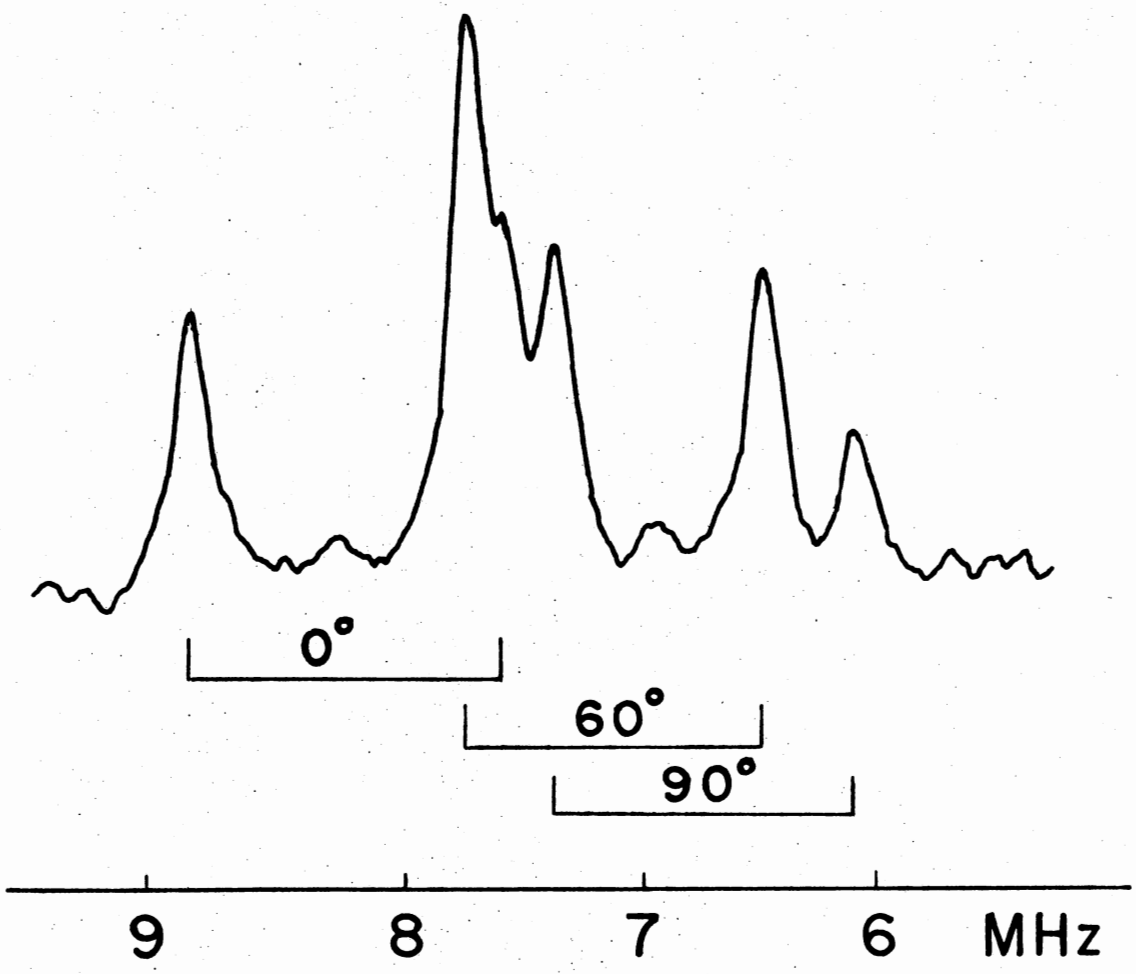

Figure 13. ENDOR Spectrum of ^{39}K Nuclei, H//[110]

nucleus with the F center electron, the eight distinct transition frequencies from the two high symmetry spectra were used in a fitting program. The 8 x 8 matrix given in Table III of Chapter IV is very general in the sense that no numerical values for the hyperfine tensor of the ^{39}K nucleus or the direction of magnetic field with respect to the crystallographic direction have been specified. Numerical values for the three hyperfine parameters were obtained by using this 8 x 8 matrix in an iterative procedure. This method consists of the following; first, an initial set of parameter values were assumed and the ENDOR frequencies corresponding to the eight distinct high symmetry experimental lines were calculated and compared to the experimental values given in Table IV, then the process was repeated a number of times as the parameters were systematically varied until the eight calculated frequencies agreed within experimental error with the eight experimental values.

More specifically the iterative technique consisted of minimizing a quantity called SUM given by

$$SUM = \sum_{i=1}^{8} [\nu_i^{exp} - \nu_i^{cal}]^2$$

where ν_i^{exp} = experiment value of ENDOR frequency and ν_i^{cal} = calculated value of ENDOR frequency. After the first calculation of SUM using the initially assumed set of parameters, one of the parameters is increased by a specified amount and all ν_i^{cal} are again obtained by diagonalization of the 8 x 8 matrices and SUM is recalculated. This SUM is compared with the previously determined SUM. If the new SUM is greater than the previously determined SUM, the value of the parameter is decreased by twice the earlier increment and all ν_i^{cal} are obtained again and another

value of SUM is calculated. This SUM is compared with the original SUM and the value of the parameter giving the smallest SUM is retained. The above procedure is repeated for each of the other two parameters before returning to the first parameter. The final set of parameters is obtained when no variation of any of the parameters results in a lowering of the SUM value. The parameters which were found to give the best fit for the first shell ^{39}K nuclei are as follows:

$$A_x (=A_y) = 13.4 \pm .07 \text{ MHz}$$

$$A_z = 16.5 \pm .07 \text{ MHz}$$

For comparison, Table IV gives the calculated and experimental ENDOR frequencies for the first shell ^{39}K nuclei. As can be seen, the agreement between calculated and experimental values is quite satisfactory.

The final values of the hyperfine parameters were then used to generate the ENDOR frequencies for different directions of the magnetic field with respect to the crystallographic directions. Figure 14 is a plot of the ENDOR frequency vs. magnetic field directions for the first shell ^{39}K nuclei and illustrates the removal of orientational degeneracies when the magnet is rotated off the high symmetry directions.

First Shell ^{19}F ENDOR

The first shell fluorines are noted for their large interaction with the F center electron. This interaction is sufficiently large to be resolved in the ESR spectrum of the F center. However, the ESR spectrum shows no angular dependence and thus the isotropic and aniso-

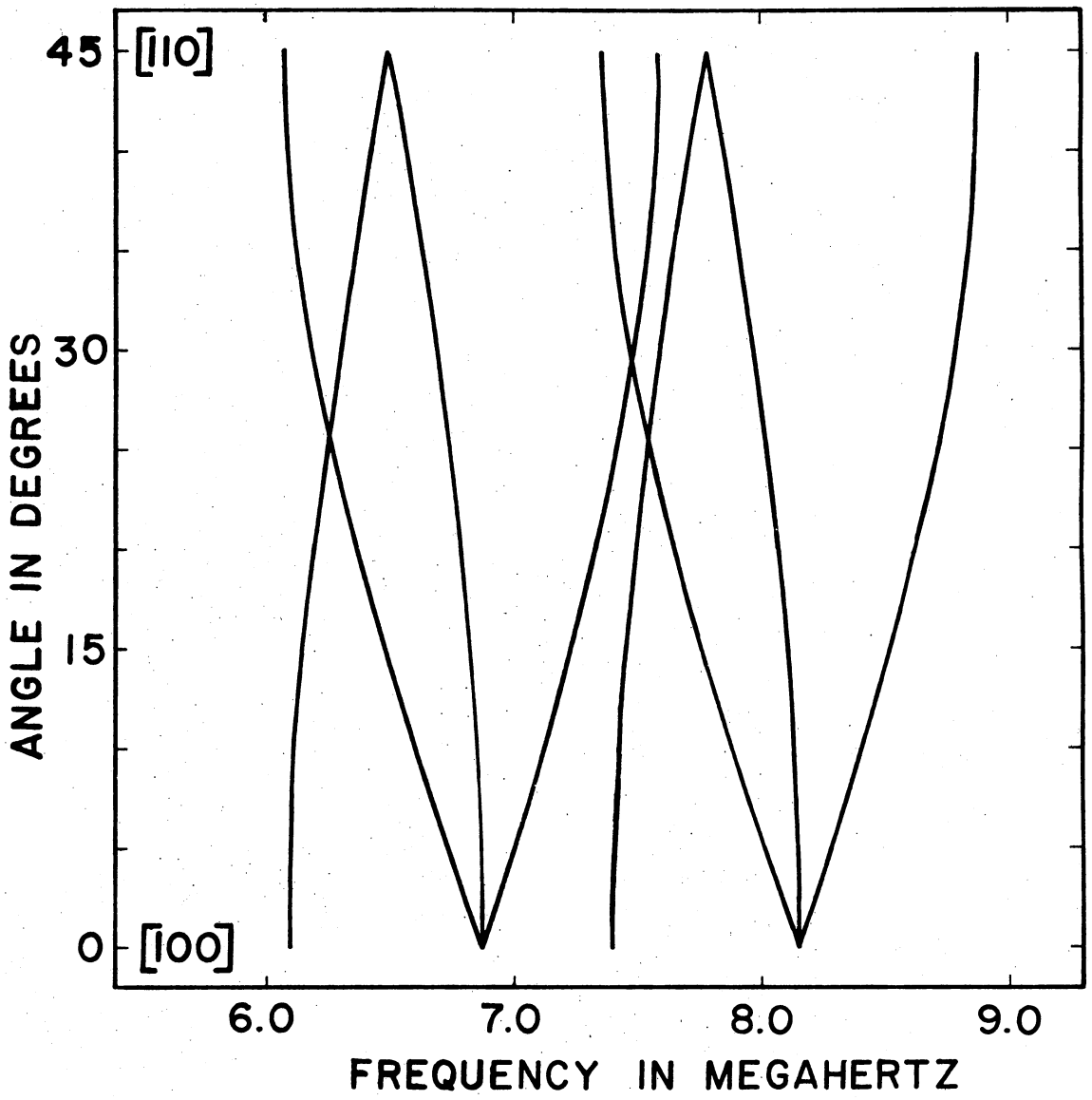

Figure 14. Computer-generated Angular Study of ^{39}K ENDOR Lines; Rotation in a (001) Plane

tropic portions of the nearest neighbor fluorine hyperfine tensor can not be determined solely from the ESR data. This information can only be obtained from the ENDOR experiment.

The ENDOR lines occur at frequencies spread over a large portion of the radio frequency spectrum because of the strong interaction between the first shell fluorine nuclei and the F center electron. Experimentally, this broad range of frequencies was scanned in steps while searching for ENDOR transitions.

For the magnetic field along a [100] direction, the results of scanning the region between 55 and 110 MHz are shown in Figures 15, 16, 17, and 18. As shown in these figures, the four lines observed in this region occur at 58.7 MHz, 74.2 MHz, 86.2 MHz, and 100.8 MHz. The two lines found at 58.7 MHz and 86.2 MHz appear very similar; both show a distinct doublet shape and both are approximately one half the intensity of the other two lines in the [100] spectrum. In addition, they are separated by the amount $2g_n\beta_n H$ (where H equal 3220 gauss). Thus these two lines form an ENDOR pair due to one type of fluorine nuclear site and are transitions within the electronic spin-up and spin-down energy levels, respectively. Similarly, the ENDOR lines at 74.2 MHz and 100.8 MHz in the [100] spectrum form a separate pair due to fluorine nuclei in a second distinct type of nuclear site. These experimental results are summarized in Figure 19.

When the magnetic field is along a [100] firection, the eight nearest neighbor fluorine nuclei can be divided into two groups. One group makes a 45° angle with the magnetic field and the other group makes a 90° angle with the field. Because of the three distinct [100]-type orientations for the F centers, there are twice as many fluorine nuclei

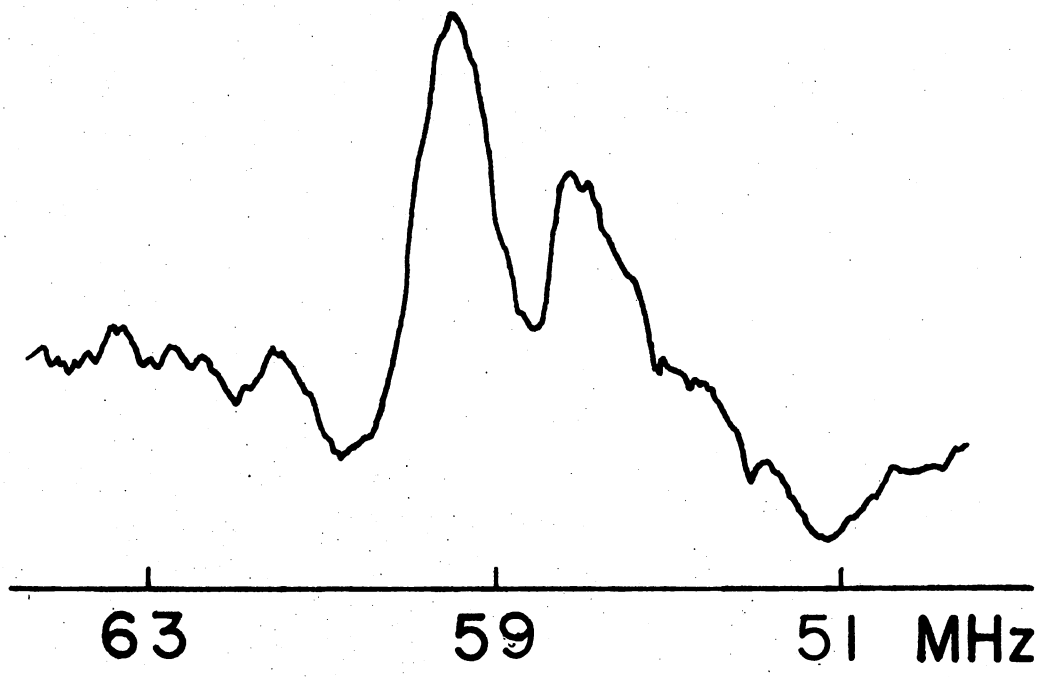

Figure 15. Low Frequency ENDOR Line of 90° Type First Shell ^{19}F Nuclei, H//[100]

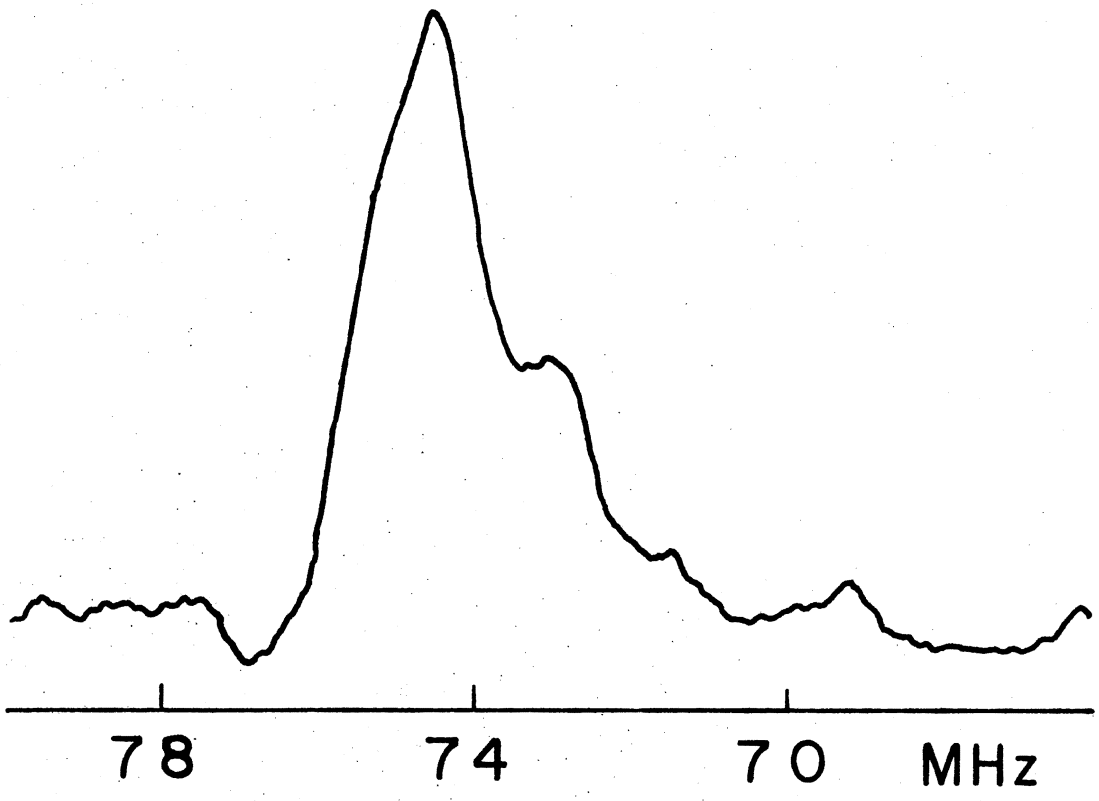

Figure 16. Low Frequency ENDOR Line of 45° Type First Shell ^{19}F Nuclei, H//[100]

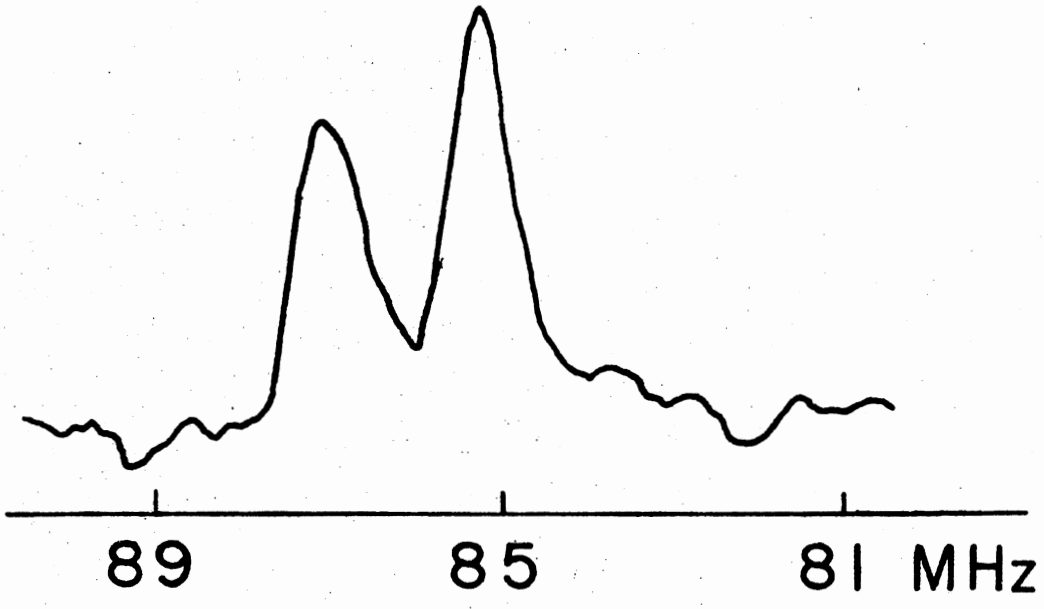

Figure 17. High Frequency ENDOR Line of 90° Type First Shell ^{19}F Nuclei, H//[100]

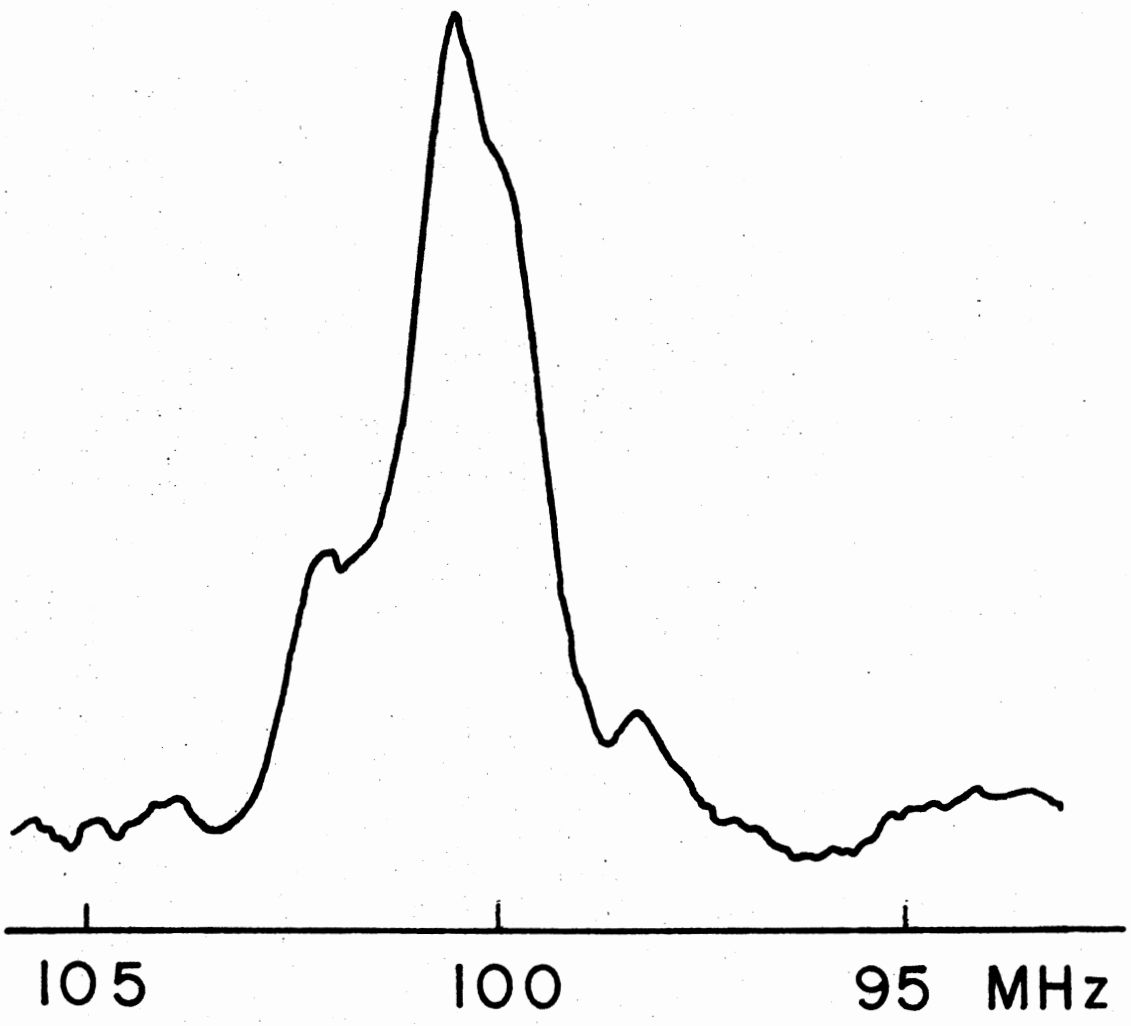

Figure 18. High Frequency ENDOR Line of 45° Type First Shell ^{19}F Nuclei, H//[100]

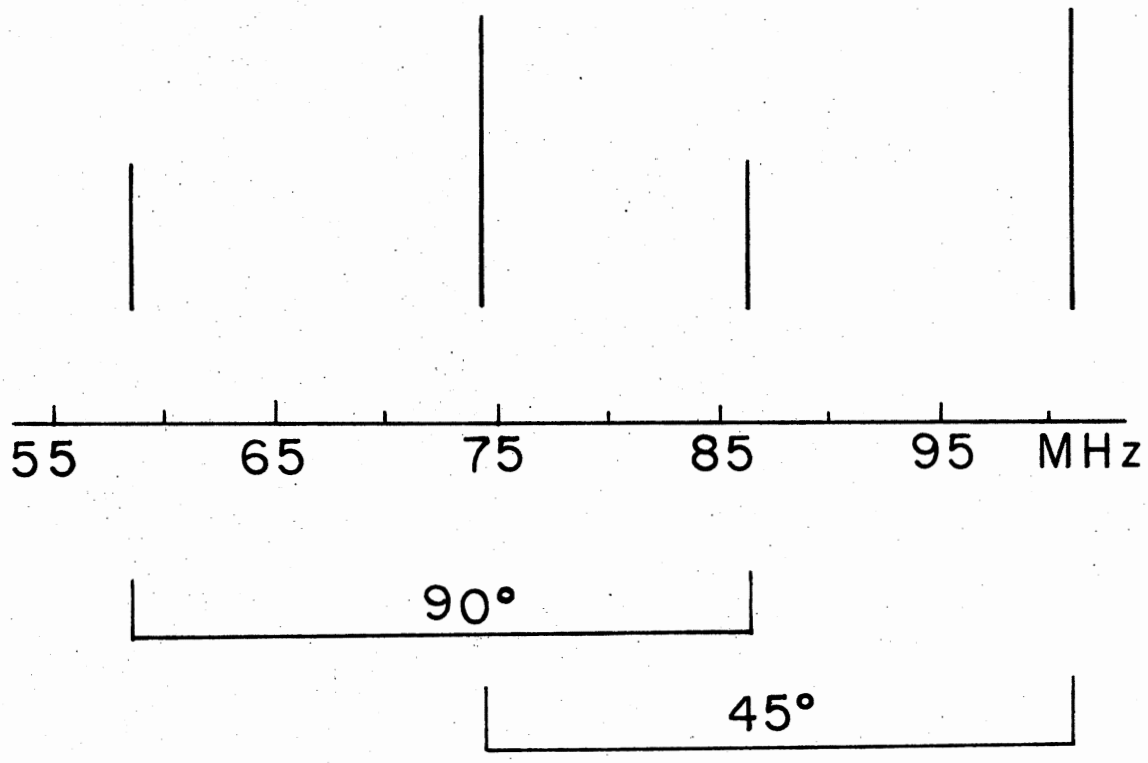

Figure 19. Stick Diagram of the First Shell ^{19}F Nuclei ENDOR Lines, H//[100]

in the 45° group as in the 90° group. Experimentally, these expectations are borne out by the data shown in Figure 19 where only two groups are found and they have a relative intensity ratio of 2:1. The more intense pair has been labeled 45° in Figure 19 and the smaller pair has been labeled 90°.

As can be seen from Figures 15, 16, 17, and 18, the nearest neighbor fluorine ENDOR lines are actually doublets. In Figures 16 and 18, the ENDOR lines are broad, and the doublet features although evident are not as pronounced. The effective ENDOR Hamiltonian as discussed in Chapter IV for the 4 vector-basis set $|M_S = \pm 1/2, M_I = \pm 1/2\rangle$ does not predict any doublet feature in the ENDOR spectra. A small quadrupole interaction could give rise to line broadening but fluorine (I = 1/2) does not have a quadrupole moment.

The origin of the doublet features in the ENDOR spectra can be explained by considering two fluorine nuclei simultaneously thus allowing for an effective nuclear-nuclear interaction in the ENDOR Hamiltonian. Such effects have been seen before (34, 9) and can be correctly accounted for by using the ENDOR Hamiltonian

$$H = g\beta \vec{H}\cdot\vec{S} + \vec{I}_1\cdot\overleftrightarrow{A}\cdot\vec{S} + \vec{I}_2\cdot\overleftrightarrow{A}\cdot\vec{S} - g_n\beta_n\vec{H}\cdot(\vec{I}_1 + \vec{I}_2)$$

where the two spins I_1 and I_2 are in equivalent sites relative to the F center. In evaluating the ENDOR frequencies resulting from this two-nucleus Hamiltonian, one must be careful to use the correct selection rules. After initially verifying that the doublet splitting observed in the [100] fluorine ENDOR spectrum from the F centers in $KMgF_3$ could be exactly predicted by this Hamiltonian, no further importance was attached to the doublet splittings. In all the subsequent analysis, only a single

nucleus Hamiltonian was used and the centers of the doublets were assumed to be the line positions.

For the magnetic field along a [110] direction, the first shell fluorine nuclei are divided into three groups--one group makes a 0° angle with the magnetic field, a second group makes a 60° angle, and the third group makes a 90° angle. The relative intensity of the ENDOR lines from these three groups are 1:4:1, respectively. These three groups give rise to six lines (three pairs) in the F center [110] ENDOR spectrum. Two of these lines are shown in Figure 20(a) and one other line is shown in Figure 20(b). In the upper portion of this figure both of the lines are doublets, but the high frequency components of each doublet overlap leaving three observable peaks. The highest frequency line of the six fell outside the frequency range of the spectrometer's sweep generator and thus was not directly observed. The [110] first shell fluorine ENDOR spectrum results are summarized in Figure 21.

Once the experimental ENDOR spectra have been obtained, the next step is to evaluate the spin Hamiltonian parameters needed to describe such spectra. The z direction of the principal axis system for the hyperfine tensor of the first shell ^{19}F nuclei is taken to be inward towards the F center vacancy. This direction of the z axis is not required by the symmetry of the nuclear site but must be true nonetheless because there is no observable splitting of the pair of ENDOR lines labeled [45°] in the [100] spectrum. The symmetry of the lattice does absolutely fix one of the other two principal axis directions. The plane formed by the F center vacancy, the nearest neighbor magnesium ions, and the particular first shell fluorine ion is a reflection plane and thus must have a principal axis perpendicular to it.

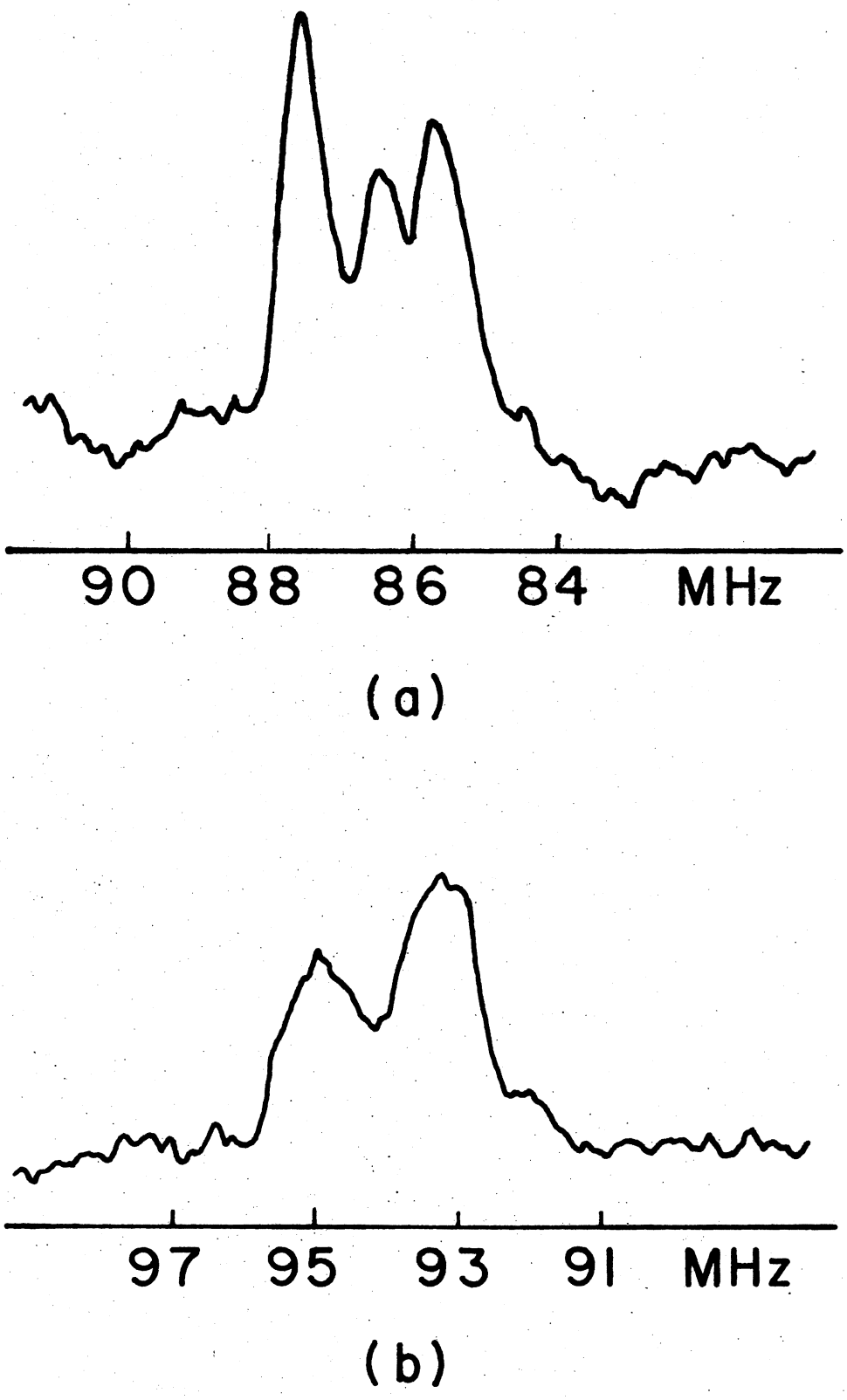

Figure 20. Partial ENDOR Spectra of First Shell ^{19}F Nuclei Showing Two Lines in (a), and One Line in (b), H//[110]

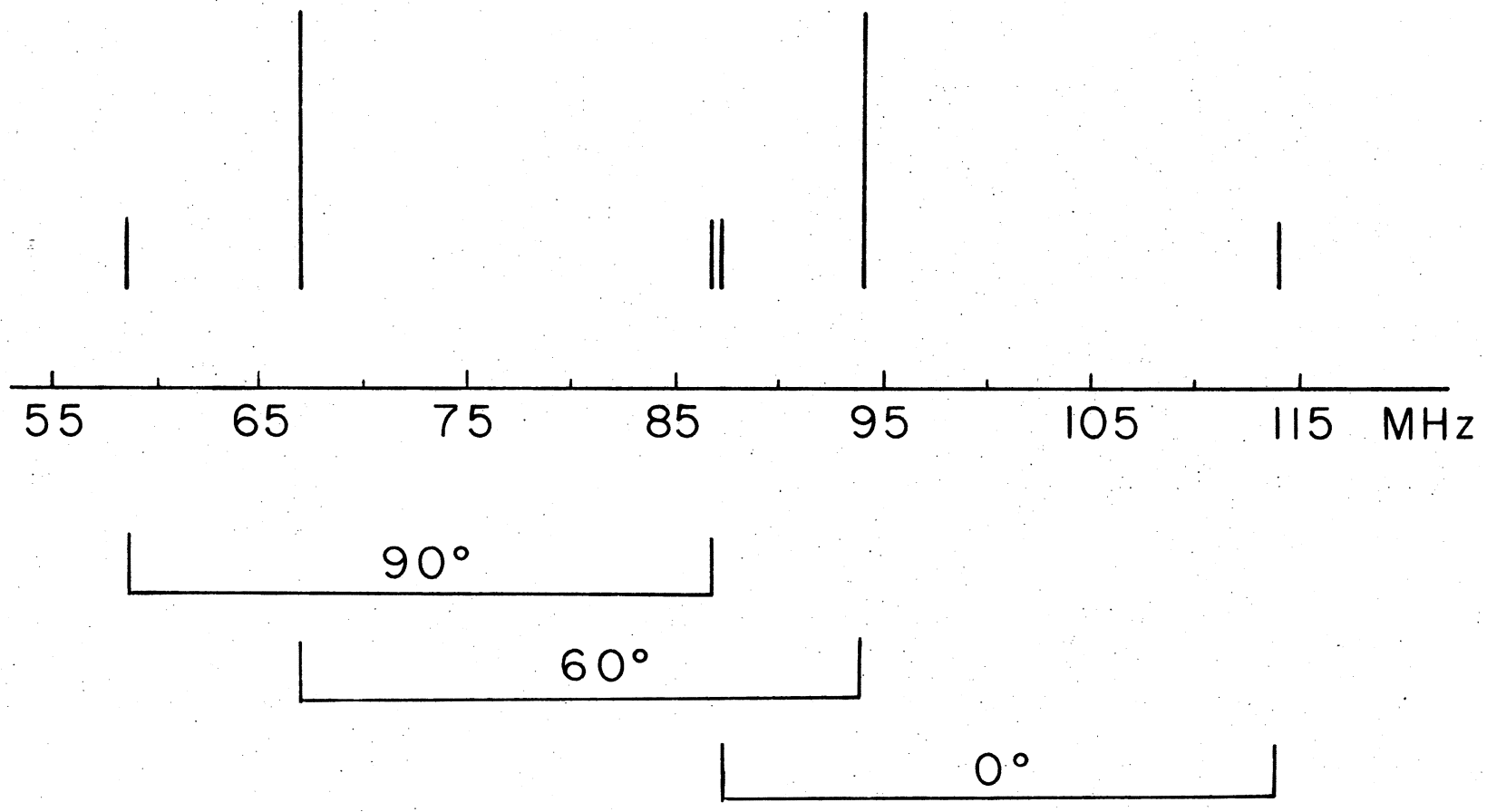

Figure 21. Stick Diagram of the First Shell ^{19}F Nuclei ENDOR Lines, H//[110]

From the crystal symmetry, it can be seen that the x and y directions of the principal axis system are not equivalent for the hyperfine tensor of the first shell ^{19}F nuclei. However, since the 90^{o} pair of the ENDOR lines in the [100] spectrum occur at the same frequencies as the 90^{o} pair of lines in the [110] spectrum, the A_x principal value of the hyperfine tensor must equal the A_y value. Hence the first shell fluorine ENDOR spectra were analyzed using only 2 parameters $A_x (=A_y)$ and A_z.

Since just two hyperfine interaction constants needed to be determined, only the 4 experimental ENDOR frequencies obtained from the [100] spectrum were used in an iterative fitting procedure. The computer program used to find the best fit parameters is essentially the same as the one previously described for the ^{39}K ENDOR analysis. Starting with a given pair of values for the two parameters $A_x (=A_y)$ and A_z, the program diagonalizes the 4 x 4 ENDOR Hamiltonian matrix for the 45^{o} and 90^{o} fluorine nuclei. The ENDOR frequencies corresponding to the observed [100] transitions were then obtained and compared with the corresponding experimental values. This procedure was repeated numerous times as the two parameter values were systematically varied till the best fit values of $A_x (=A_y)$ and A_z were obtained. These best fit values are

$$A_x (=A_y) = 145 \pm 1 \text{ MHz}$$

$$A_z = 201 \pm 1 \text{ MHz} .$$

The experimental ENDOR frequencies from which these parameter values were obtained are listed in Table V along with the calculated ENDOR

TABLE V

OBSERVED AND CALCULATED FREQUENCIES OF FIRST SHELL ^{19}F ENDOR SPECTRUM, H//[100]

Observed Frequency MHz (± .2 MHz)	Calculated Frequency MHz	Transition
58.7	58.79	$\|M_S = +1/2, M_I = -1/2\rangle \leftrightarrow \|M_S = +1/2, M_I = +1/2\rangle$
74.2	74.26	$\|M_S = +1/2, M_I = -1/2\rangle \leftrightarrow \|M_S = +1/2, M_I = +1/2\rangle$
86.2	86.21	$\|M_S = -1/2, M_I = -1/2\rangle \leftrightarrow \|M_S = -1/2, M_I = +1/2\rangle$
100.8	101.05	$\|M_S = -1/2, M_I = -1/2\rangle \leftrightarrow \|M_S = -1/2, M_I = +1/2\rangle$

frequencies using this final set of parameters. A computer was then used to generate ENDOR frequencies for different directions of the magnetic field with respect to the crystallographic directions. A graph was plotted with ENDOR frequencies vs. direction of the magnetic field. This is shown in Figure 22.

Second Shell ^{19}F ENDOR

The second shell fluorine nuclei are divided into two types (see Figure 1). Both types are the same distance from the F center vacancy if the surrounding lattice remains undistorted. In one of the two cases there is a Mg^{++} ion between the second shell fluorine and the F center vacancy. The fluorines of this type are labeled shell 2A. The other case, labeled shell 2B, has no intervening ions between the fluorine and the F center vacancy.

Since the second shell fluorines are more distant, their hyperfine interactions are much smaller than for the first shell fluorines. A series of weak ENDOR lines were observed in the frequency range from 4 MHz to 22 MHz and these have been assigned to the fluorine 2A and 2B shells. These ENDOR lines were arranged symmetrically about the fluorine free spin value (12.9 MHz for a field of 3220 gauss) and Table VI lists the observed frequencies for the case when the magnetic field is along a [100] direction.

Inspection of the crystal structure shows that shell 2A is divided into two groups for the magnetic field in a [100] direction. These two groups are 0° and 90° types with the 90° group twice as large as the 0° group. The z direction of the principal axis system for the hyperfine tensor of shell 2A is taken to be toward the F center vacancy and the x and y directions are equivalent and fixed by symmetry.

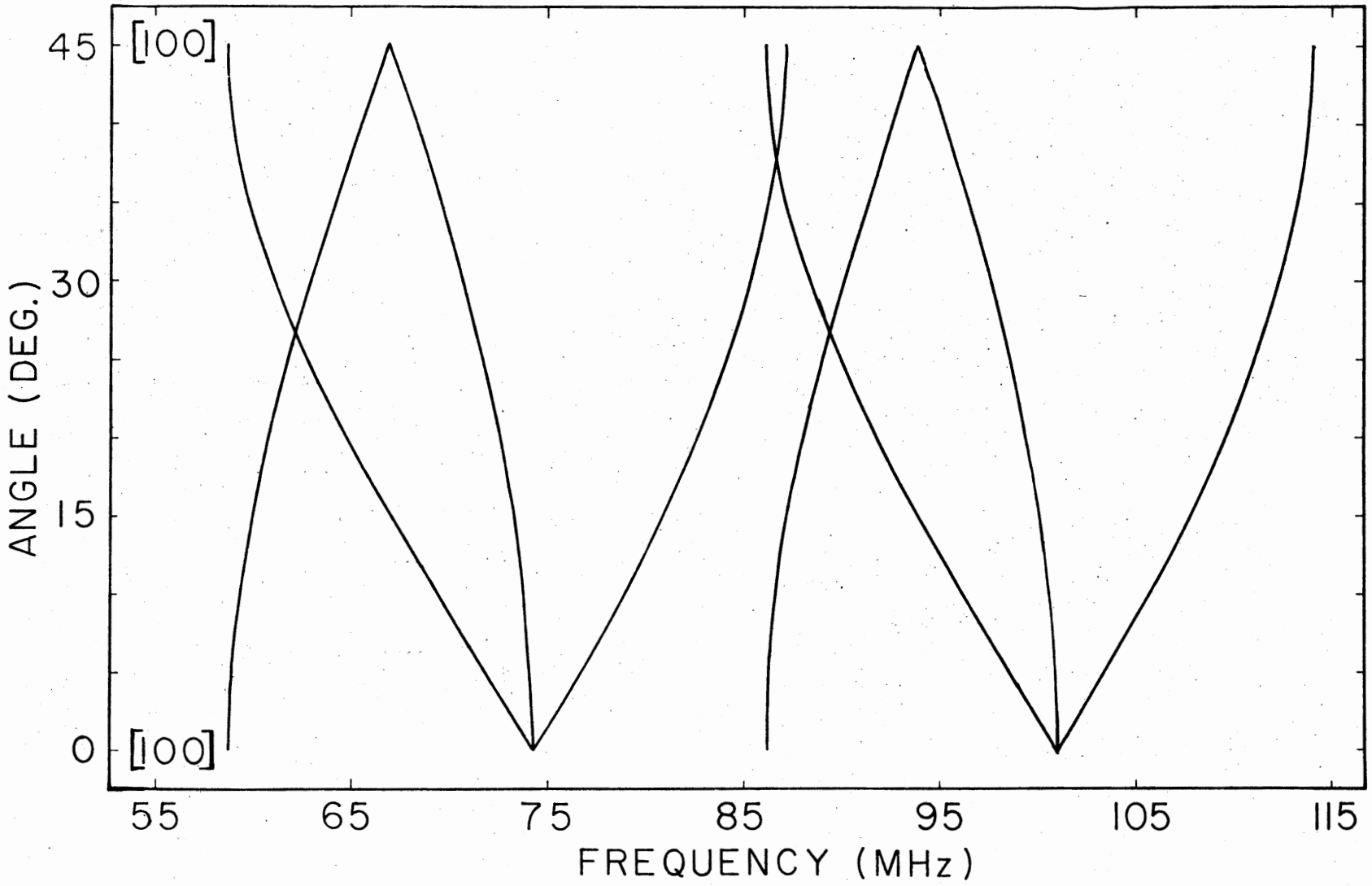

Figure 22. Computer-generated Anaular Study of First Shell ^{19}F Nuclei ENDOR Lines; Rotation in a (001) Plane

TABLE VI

OBSERVED AND CALCULATED FREQUENCIES OF THE SECOND SHELL ^{19}F ENDOR SPECTRUM

[100] Direction

Fluorine Shell	Observed Frequency MHz (± .3 MHz)	Calculated Frequency MHz	Transition
2A	20.0	20.2	$\|M_S = -1/2, M_I = -1/2\rangle \leftrightarrow \|M_S = -1/2, M_I = +1/2\rangle$
2A	17.2	17.2	$\|M_S = -1/2, M_I = -1/2\rangle \leftrightarrow \|M_S = -1/2, M_I = +1/2\rangle$
2B	16.7	16.8	$\|M_S = -1/2, M_I = -1/2\rangle \leftrightarrow \|M_S = -1/2, M_I = +1/2\rangle$
2B	14.5	14.4	$\|M_S = -1/2, M_I = -1/2\rangle \leftrightarrow \|M_S = -1/2, M_I = +1/2\rangle$
2B	11.4	11.3	$\|M_S = +1/2, M_I = -1/2\rangle \leftrightarrow \|M_S = +1/2, M_I = +1/2\rangle$
2B	8.8	8.5	$\|M_S = +1/2, M_I = -1/2\rangle \leftrightarrow \|M_S = +1/2, M_I = +1/2\rangle$
2A	5.4	5.5	$\|M_S = +1/2, M_I = -1/2\rangle \leftrightarrow \|M_S = +1/2, M_I = +1/2\rangle$

Shell 2B also is divided into two groups, 0^{o} and 90^{o}, with the 90^{o} group being twice as intense when the magnetic field is in a [100] direction. The z direction of the shell 2B hyperfine interaction is directed toward the F center vacancy, but x and y although fixed in direction by the lattice symmetry need not be equivalent. Experimentally, the x and y principal axis directions for shell 2B are indistinguishable.

Since both shells 2A and 2B are divided into two groups for the magnetic field along a [100] direction, there must be four pairs of ENDOR lines in the spectrum for this orientation. Seven of these eight lines are the experimental lines listed in Table VI. The eighth line is buried beneath the much larger first shell ^{39}K spectrum described in the first section of this chapter. Figure 23 illustrates the shells 2A and 2B ENDOR spectra. Experimentally, the spectra due to the two shells cannot be distinguished. Shell 2A has been arbitrarily assigned to the more widely split set of ENDOR lines as shown in Figure 23, because greater spin density is expected to be transferred to the 2A nuclei by the intervening Mg^{++} ion. Shell 2B has no intervening ion and thus should have a smaller hyperfine interaction.

The Hamiltonian parameters for shells 2A and 2B were determined in a manner analogous to that used for the first shell potassium and fluorine nuclei. The data from the [100] ENDOR spectrum listed in Table VI was used in the fitting procedure and the results are as follows:

Shell 2A:

$$A_x \ (=A_y) = 8.7 \pm .5 \text{ MHz}$$

$$A_z = 14.6 \pm .5 \text{ MHz}$$

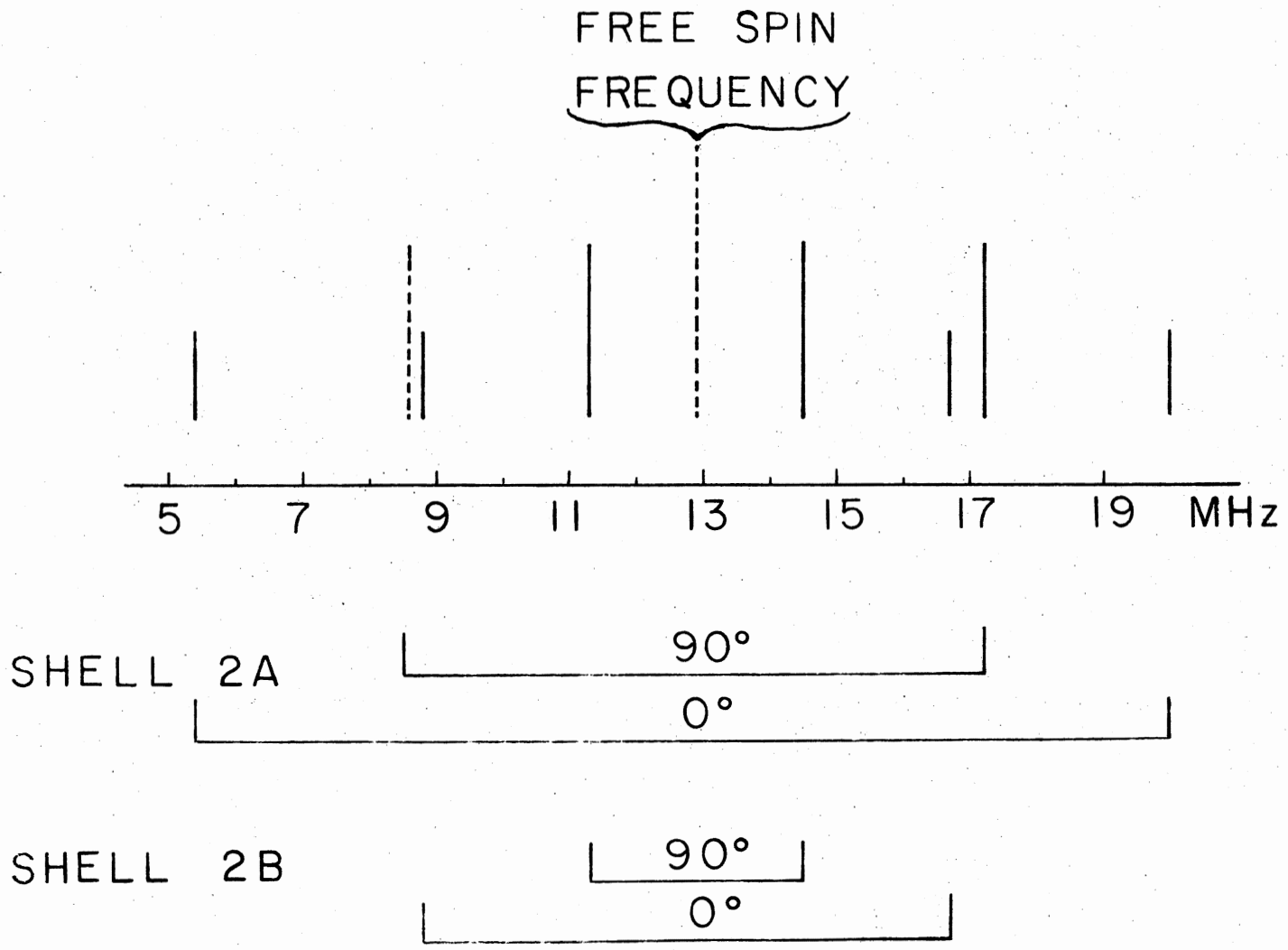

Figure 23. Stick Diagram of Second Shell ^{19}F Nuclei ENDOR Lines, H//[100]

Shell 2B:

$$A_x \ (=A_y) = 3.1 \pm .5 \text{ MHz}$$

$$A_z = 7.9 \pm .5 \text{ MHz}$$

These two sets of parameters were used to calculate the angular dependence of the ENDOR spectrum for shells 2A and 2B. The resulting plot of ENDOR frequency vs. magnetic field direction is shown in Figure 24. In this figure, shell 2A is represented by solid lines and shell 2B is represented by dashed lines.

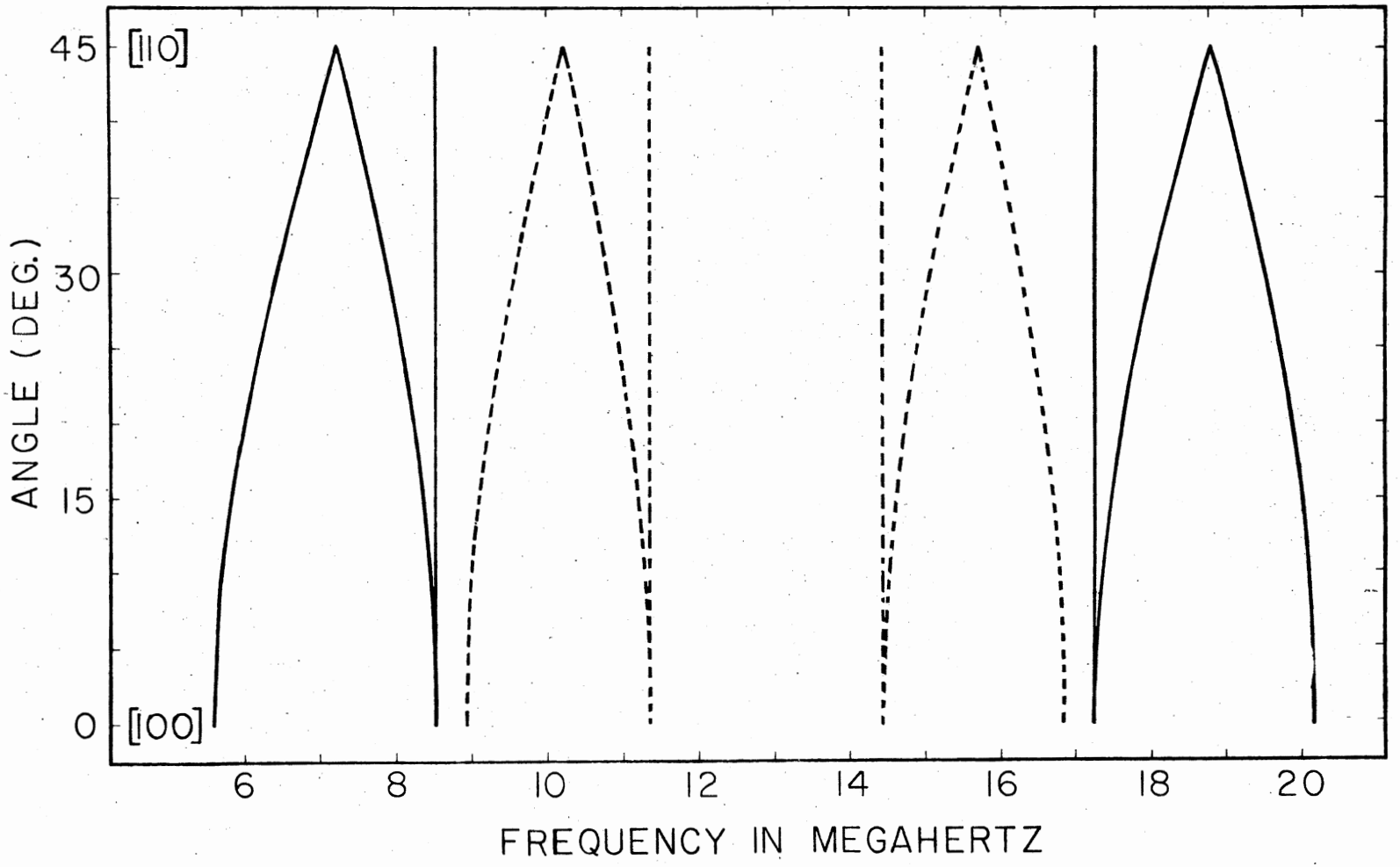

Figure 24. Computer-generated Angular Study of Second Shell ^{19}F Nuclei ENDOR Lines; Rotation in a (001) Plane

CHAPTER VI

INTRINSIC V_K CENTER IN $RbMgF_3$

Brief exposures of halide materials to ionizing radiation is known to result in the formation and trapping of holes within the lattice. These holes are formed on an anion when the radiation causes removal of one of the valence band electrons. Immediately after formation, the hole minimizes its energy and becomes self-trapped by distributing itself over two adjacent anions. The resulting self-trapped hole is then in the form of an X_2^- molecule (where X represents the halogen) and are labeled V_K centers. The stability of these molecular ions depends upon the crystal structure, halide interionic separation, and the specific halogen electronic structure. Typically, V_K centers in halide materials are stable only up to temperatures in the range 100-200 K.

Experimental Results

As described in Chapter I, the $RbMgF_3$ samples used in the present investigation have an hexagonal crystal structure. Figure 2 shows that the fluorines form equilateral triangles lying in the c-axis planes and Koumvakalis (27) has shown that V_K centers are formed from pairs of fluorines located at corners of these equilateral triangles. A major goal of the present investigation was to verify this assignment of V_K centers only to pairs of fluorines lying in the c-axis planes by using the much higher resolution ESR technique. With ESR, one is able to

examine separately spectra due to V_K centers having various orientations with respect to the crystal axes.

Following brief irradiations using the Van de Graaff accelerator, intense ESR spectra showing the distinct characteristics of F_2^- molecules were observed in the $RbMgF_3$ samples. In describing the observed spectra, use will be made of the set of three crystal axes $\vec{a}_1$, $\vec{a}_2$, and $\vec{a}_3$ which lie in the c-plane and which make 120° angles with each other. The ESR spectrum obtained at 77 K when the magnetic field is parallel to the $\vec{a}_1$ crystal axis is shown in Figure 25. The lines in this spectrum can be divided into two groups, and this is the behavior expected if the V_K centers do lie only in the c-axis plane.

For F_2^- molecules, the separation of the outer pair of lines is given approximately by $A_z \cos^2\theta$ (if θ is between 0° and 75°) where θ is the angle between the magnetic field direction and the molecular axis. The expectation from the work of Koumvakalis (27) was that the two groups observed in Figure 25 would correspond to $\theta = 0^\circ$ and $\theta = 60^\circ$. Using the above expression for the separation of the outer pair of lines from each of the two groups in Figure 25 shows that the angles $\theta = 0^\circ$ and $\theta=60^\circ$ are indeed appropriate and thus have been used as labels in the figure. There are no lines in Figure 25 which could be attributed to V_K centers having a component of orientation along the c-axis.

The spectra shown in Figures 26 and 27 were taken with the magnetic field in the c-axis plane. The magnetic field is 15° away from the $\vec{a}_1$ axis in Figure 26 and V_K centers located on each of the three sides of the equilateral triangle can be easily distinguished. The three resulting groups of lines are labeled $\theta = 15^\circ$, $\theta = 45^\circ$, and $\theta = 75^\circ$. The central lines are not shown in the stick diagram in Figure 26 because of

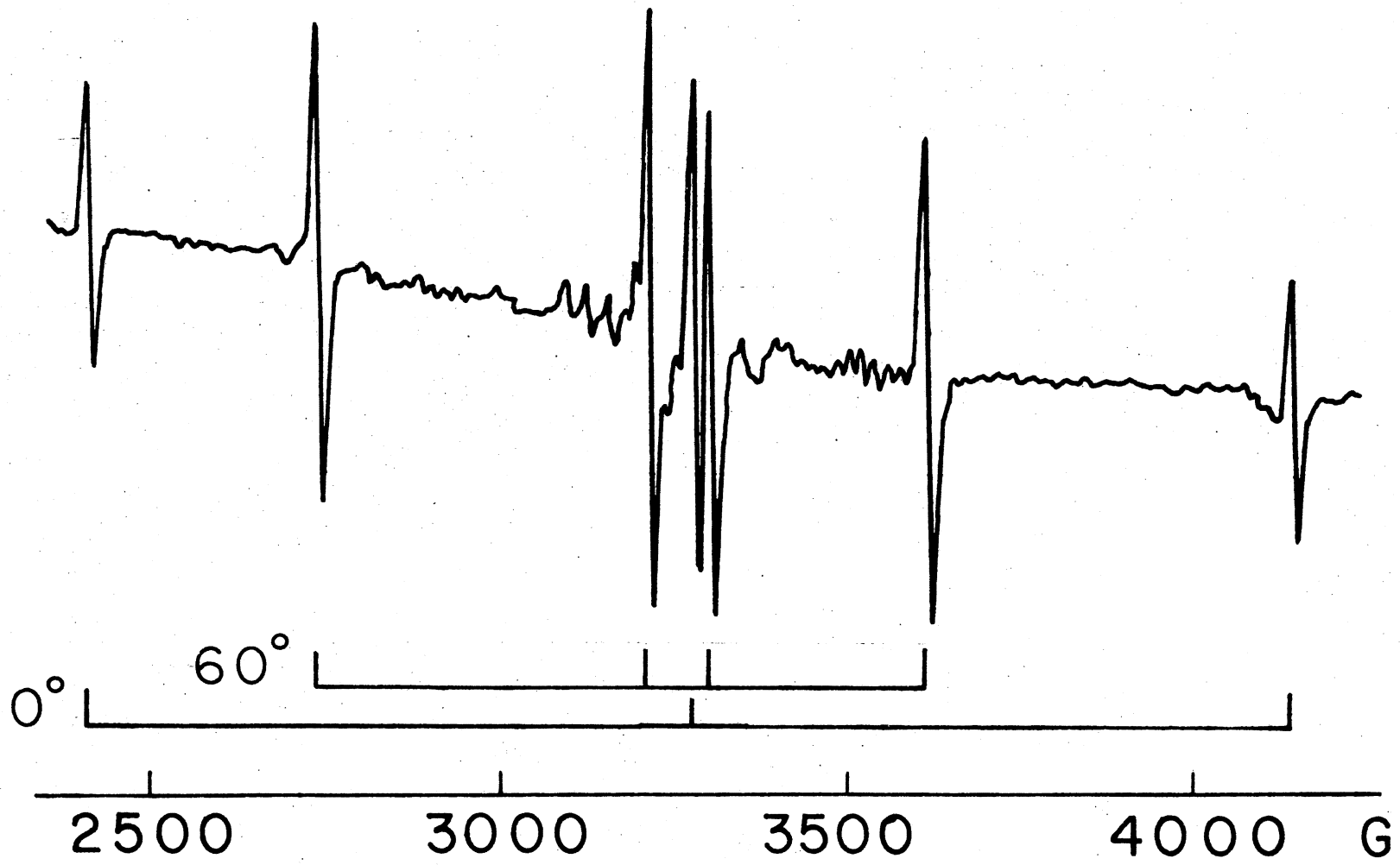

Figure 25. ESR Spectrum of the Intrinsic V_K Center in $RbMgF_3$, $\vec{H}//\vec{a}_1$

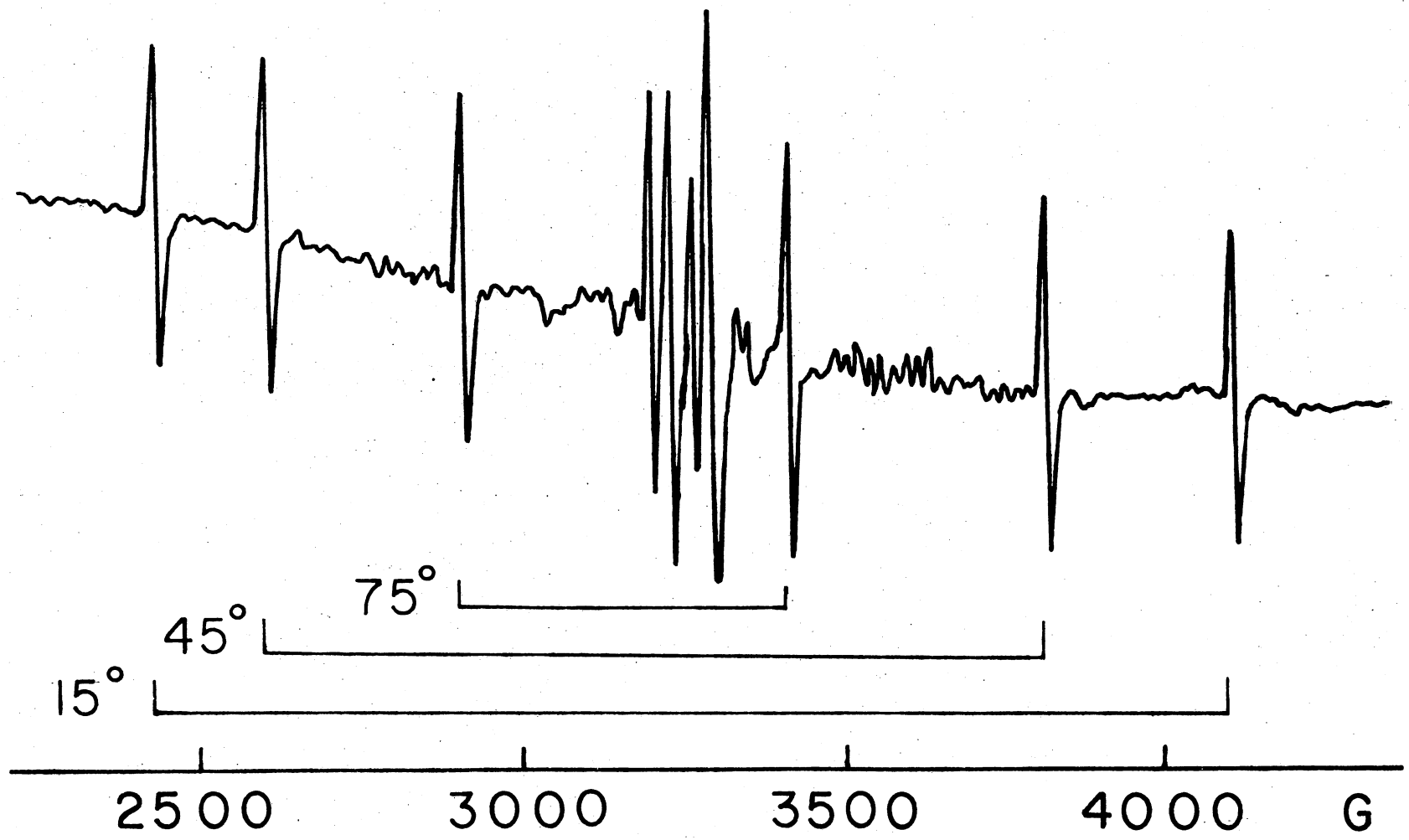

Figure 26. ESR Spectrum of the Intrinsic V_K Center in $RbMgF_3$, $\vec{H}$ Makes 15° Angle With $\vec{a}_1$

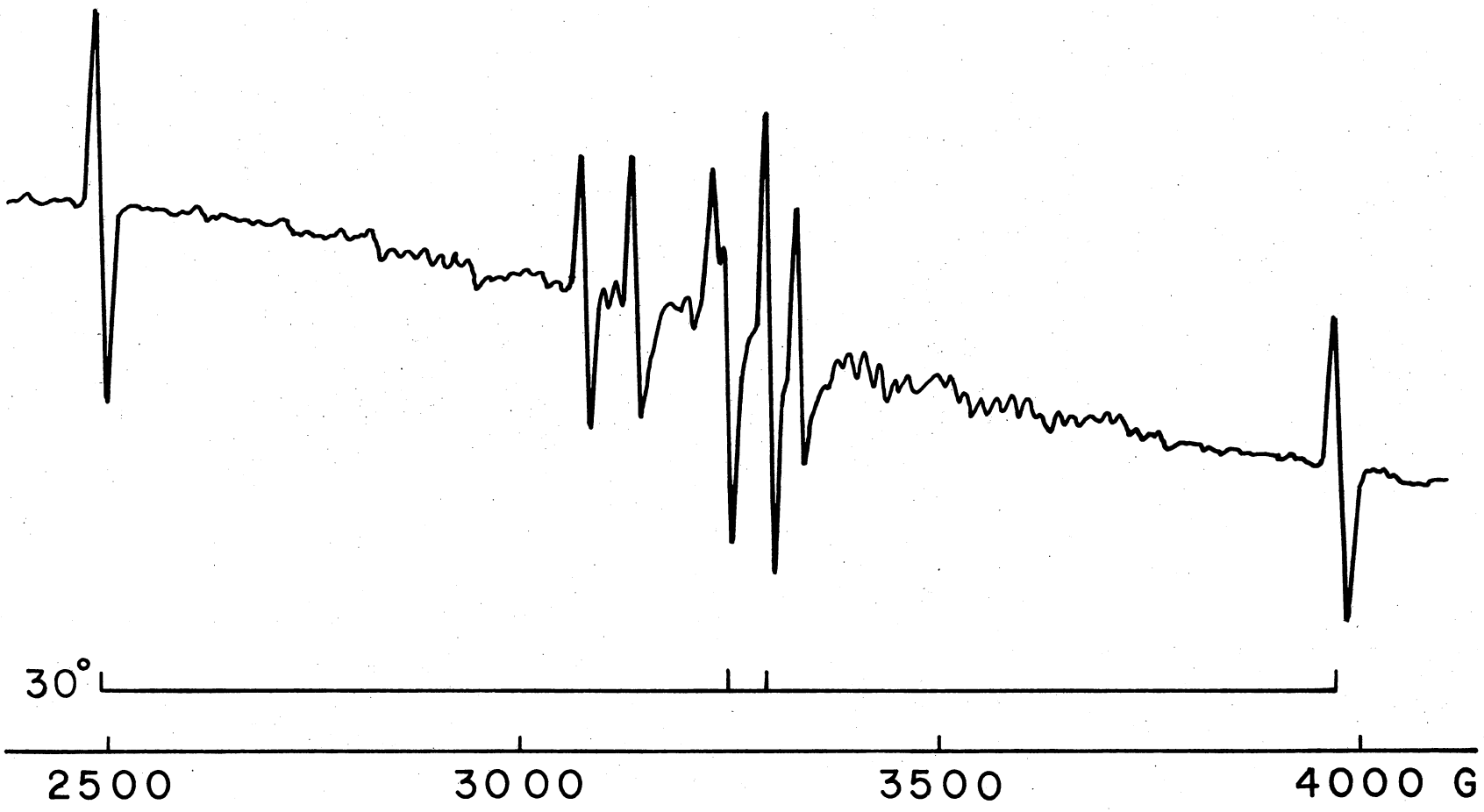

Figure 27. ESR Spectrum of the Intrinsic V_K Center in $RbMgF_3$, $\vec{H}$ Makes 30° Angle With $\vec{a}_1$

overlapping behavior.

In the case of Figure 27, the magnetic field is directed 30° away from the $\vec{a}_1$ axis (i.e., the magnetic field bisects the equilateral triangle formed by the fluorines). Again, there are two groups of lines in the spectrum, one corresponding to $\theta = 30^{\circ}$ and one corresponding to $\theta = 90^{\circ}$. Final proof that the V_K centers were perpendicular to the c-axis was obtained from a spectrum (shown in Figure 28) taken with the magnetic field parallel to the c-axis. In this spectrum, all the V_K centers formed a single group which was characterized by $\theta = 90^{\circ}$.

A series of three minute pulse anneals was undertaken to determine the thermal stability of the V_K centers. The sample was held at progressively higher temperatures for three minutes and, in between anneals, was returned to the 89 K monitoring temperature where the concentration of V_K centers was measured. The results of this thermal stability study are shown in Figure 29 and the decay temperature (the temperature at which half the centers have decayed) is seen to be approximately 134 K.

Spin Hamiltonian Analysis

The spin Hamiltonian used in the analysis of the V_K center ESR spectra is as follows:

$$H = \beta \vec{S} \cdot \overleftrightarrow{g} \cdot \vec{H} + \vec{I}_1 \cdot \overleftrightarrow{A}_1 \cdot \vec{S} + \vec{I}_2 \cdot \overleftrightarrow{A}_2 \cdot \vec{S} - g_n \beta_n \vec{H} \cdot (\vec{I}_1 + \vec{I}_2)$$

Since there is no evidence to the contrary, it was assumed that $|\vec{A}_1| = |\vec{A}_2|$. Because of the small splitting of the inner pair of lines for the 60° orientation shown in Figure 25, a bent bond angle parameter ϕ was included in the specification of the hyperfine tensors principal axes. In a manner similar to Hall (20), the z axis for each of the two

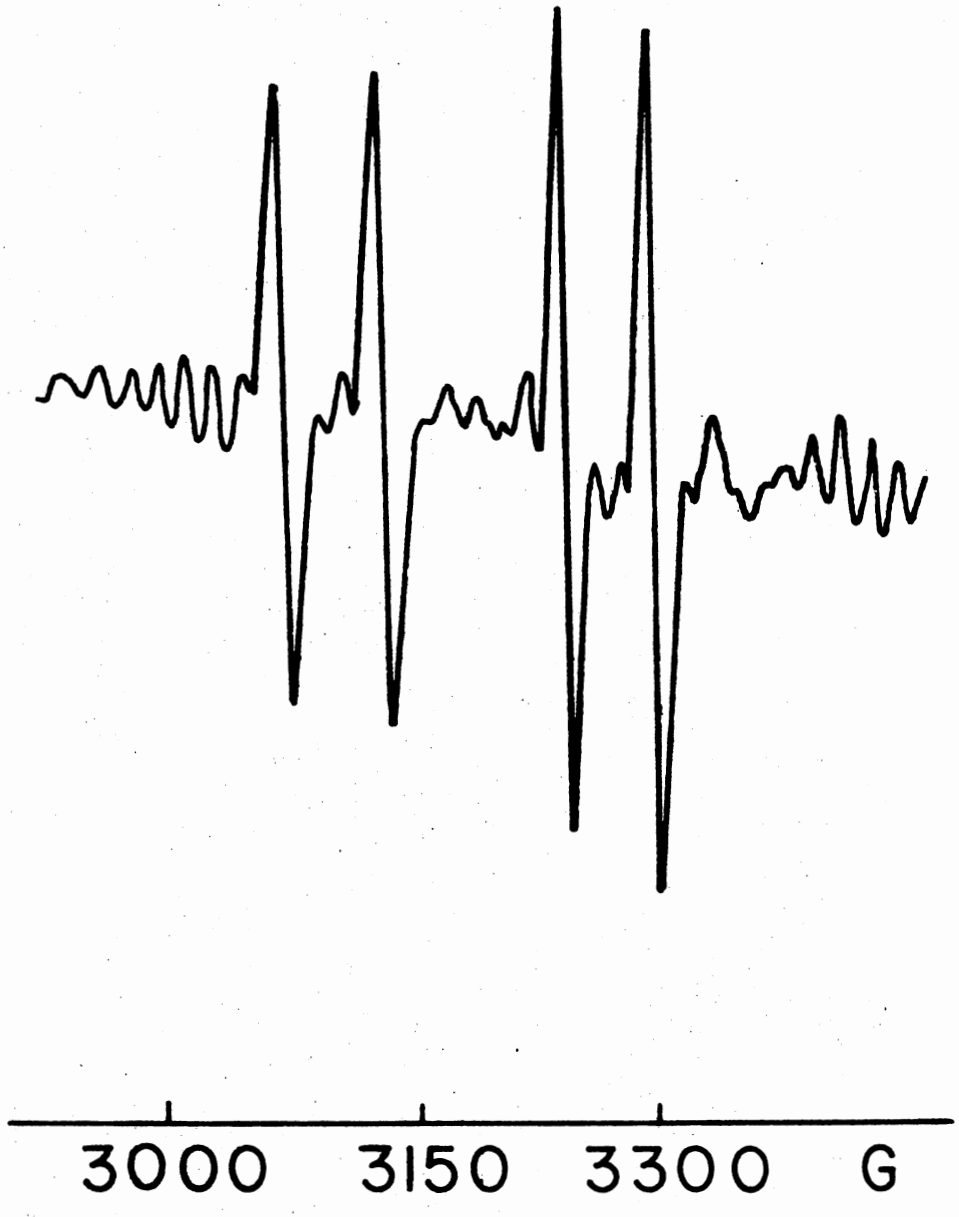

Figure 28. ESR Spectrum of the Intrinsic V_K Center in $RbMgF_3$, H//c-axis

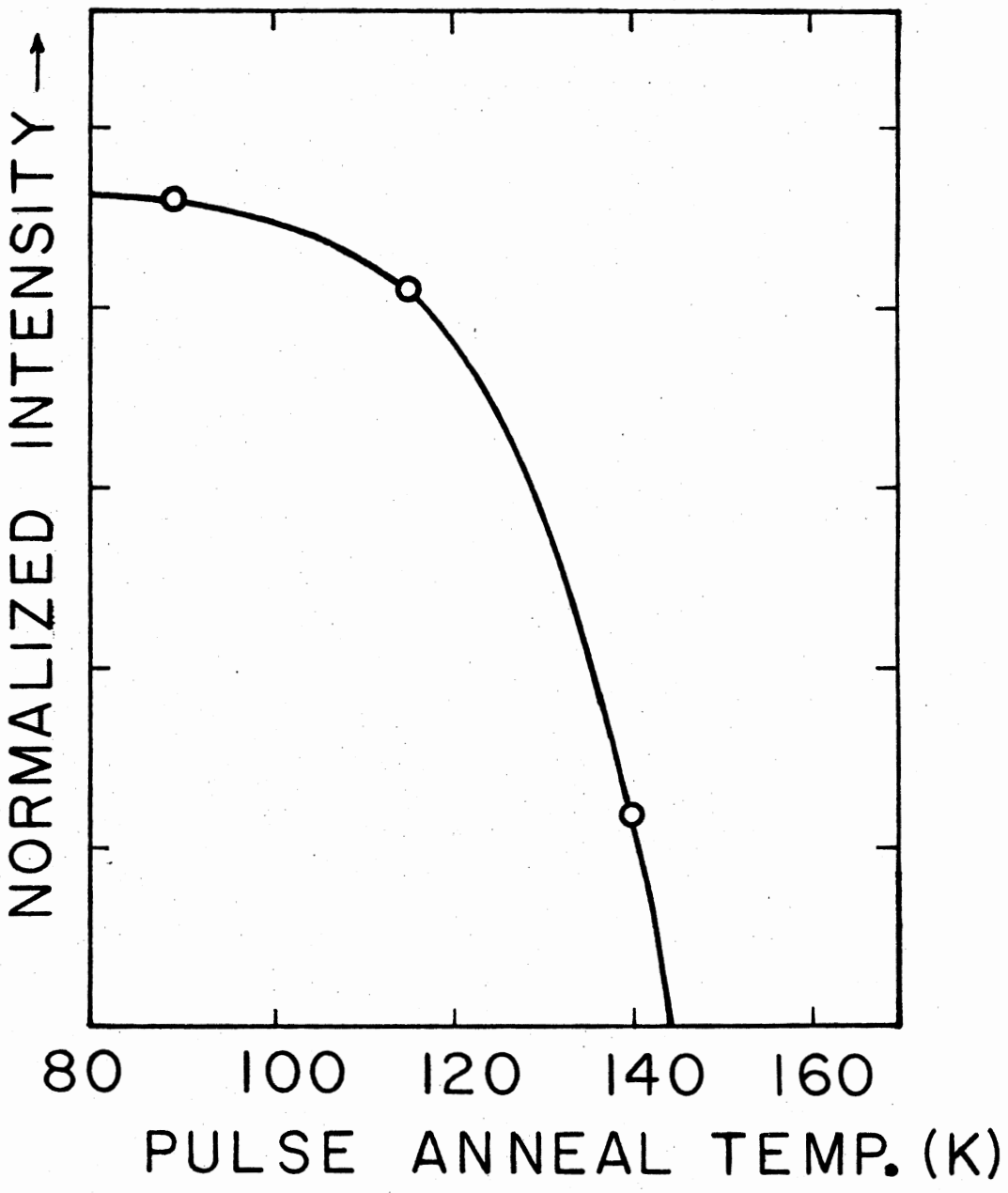

Figure 29. Pulse Anneal Study of the Intrinsic V_K Center in $RbMgF_3$

hyperfine tensors was taken to deviate an amount ϕ from the internuclear axis of the V_K center molecule. The y axis was taken to be parallel to the c-axis.

The g tensor principal axes reflect the overall symmetry of the V_K center and thus does not require a bent bond angle parameter. The z axis of the g tensor is parallel to the internuclear axis of the molecule and the y axis is parallel to the crystal c-axis.

Data from Figures 25, 26, 27, and 28 were used in an iterative procedure to find the best set of spin Hamiltonian parameters for the V_K center in $RbMgF_3$. The fitting procedure was similar to those described in the preceding chapter for the ENDOR parameters. The results of this analysis are given below.

$$g_x = 2.019$$

$$g_y = 2.0232$$

$$g_z = 2.0020$$

$$A_x = 280 \text{ MHz}$$

$$A_y = 280 \text{ MHz}$$

$$A_z = 2425 \text{ MHz}$$

$$\phi = 3.3^{\circ}$$

CHAPTER VII

CONCLUSIONS

This ENDOR investigation of the F center in $KMgF_3$ has resulted in the determination of hyperfine interaction constants of the first and second shells of ^{19}F nuclei and of the first shell of ^{39}K nuclei. As stated earlier the values of hyperfine constants for the first shell ^{19}F nuclei are

$$A_x\ (=A_y) = 145 \text{ MHz}$$

$$A_z = 201 \text{ MHz}$$

These give a value of 163.7 MHz (or 58.5 gauss) for the isotropic part of the hyperfine interaction. The values of hyperfine interaction constants for the first shell ^{39}K nuclei as quoted earlier are

$$A_x\ (=A_z) = 13.5 \text{ MHz}$$

$$A_z = 16.5 \text{ MHz}$$

and the isotropic part of the hyperfine interaction for ^{39}K nuclei is 14.5 MHz (or 5.2 gauss).

Four ^{39}K nuclei (I = 3/2) surround an F center and split each of the spin-up and spin-down states into 13 energy levels giving rise to 13 ESR transitions with a separation of 5.2 gauss between consecutive

transitions if one ignores the small anisotropic effects. This results in a total separation of 12 x 5.2 = 62.4 gauss and gives a linewidth of 31.2 gauss at half maximum. Thus the hyperfine interaction of the first shell ^{39}K nuclei accounts for about 60% of the observed 50 gauss ESR linewidth. The rest of the broadening comes mainly from the hyperfine interactions of the first shell ^{19}F nuclei with additional smaller contributions from second and more distant shells of ^{19}F nuclei.

Table VII lists the values of the isotropic part of the hyperfine interaction constants for the first shell ^{19}F nuclei and ^{39}K nuclei and compares them with the theoretical values obtained from the two cases considered by Harker (16).

TABLE VII

COMPARISON OF THEORETICAL AND EXPERIMENTAL VALUES OF THE ISOTROPIC HYPERFINE INTERACTION CONSTANTS FOR FIRST SHELL ^{39}K AND ^{19}F NUCLEI. THE VALUES ARE GIVEN IN UNITS OF GAUSS

Nucleus	Theor. (Case 1)	Theor. (Case 2)	Exp't.
^{39}K	9.4	12	5.2
^{19}F	77	70	58.5

Future studies of the F center in $KMgF_3$ might include:

(1) An ENDOR investigation to determine the hyperfine interaction parameters of the 10.1% abundant ^{25}Mg (I = 5/2) nuclei.

(2) An ENDOR study of hyperfine interaction constants of the

third shell fluorine nuclei.

The ESR part of the present work has resulted in the characterization of the intrinsic self-trapped hole center (V_K center) in $RbMgF_3$. The orientation of the V_K center with respect to the crystal axis system has been ascertained and the decay temperature and hyperfine interaction parameters have been determined. The V_K center in $RbMgF_3$ decays at approximately 134 K. The following topics are suggested for further study in $RbMgF_3$.

(1) An ESR characterization of perturbed V_K centers (V_{KA} centers),

(2) an ESR investigation of intrinsic and perturbed fluorine interstitial centers (H and H_A centers).

SELECTED BIBLIOGRAPHY

1. Feher, G., Phys. Rev. 103, 834 (1956).

2. Feher, G., Phys. Rev. 114, 1219 (1959).

3. Holton, W. C., and H. Blum, Phys. Rev. 125, 89 (1962).

4. Holton, W. C., H. Blum and C. P. Slichter, Phys. Rev. Letters 5, 197 (1960).

5. Kaplan, R., and P. J. Bray, Phys. Rev. 129, 1919 (1963).

6. Seidel, H. and H. C. Wolf, Physics of Color Centers, Edited by W. B. Fowler (1968), Academic Press.

7. Unruh, W. P. and J. W. Culvahouse, Phys. Rev. 154, 861 (1967).

8. Halliburton, L. E., D. L. Cowan and L. V. Holroyd, Phys. Rev. B 12, 3408 (1975).

9. Unruh, W. P., L. G. Nelson, J. T. Lewis and J. L. Kolopus, J. Phys. C: Solid St. Phys. 4, 2992 (1971).

10. Känzig, W., Phys. Rev. 99, 1890 (1955).

11. Castner, T. G. and W. Känzig, Phys. Chem. Solids 3, 178 (1957).

12. Castner, T. G., W. Känzig, and T. O. Woodruff, Nuovo Cimento Suppl. (10) 7, 612 (1958).

13. Woodruff, T. O., and W. Känzig, Phys. Chem. Solid 5, 268 (1958).

14. Schoemaker, D., Phys. Rev. B 7, 786 (1965).

15. Hall, T. P. P. and A. Leggeat, Solid State Communications 7, 1657 (1969).

16. Harker, A. H., J. Phys. C 6, 3349 (1973).

17. Modine, F. A. and E. Sonder, J. Phys. C: Solid State Phys. 7, 204 (1974).

18. Young, M. A., E. E. Kohnke, and L. E. Halliburton, J. Phys. C, Solid State Phys. 9, 3515 (1976).

19. Lee, K. H., Ph.D. Thesis, Oklahoma State University, 1975.

20. Hall, T. P. P., Brit. J. Appl. Phys. 17, 1011 (1966).

21. Riley, C. R. and W. A. Sibley, Phys. Rev. B 1, 2789 (1970).

22. Lewis, J. T., J. L. Kolopus, E. Sonder and M. M. Abraham, Phys. Rev. B 7, 810 (1973).

23. Rhoads, J. E., B. H. Rose and L. E. Halliburton, J. Phys. Chem. Solids 76, 346 (1976).

24. Rhoads, J. E., B. H. Rose and L. E. Halliburton, Phys. Rev. B 11, 5115 (1975).

25. Rose, B. H., J. E. Rhoads, and L. E. Halliburton, Phys. Rev. B 14, 3583 (1976).

26. Shafer, M. W. and T. R. McGuire, J. Phys. Chem. Solids 30, 1989 (1969).

27. Koumvakalis, N., Ph.D. Thesis, Oklahoma State University (1976).

28. Wertz, J. E. and J. R. Bolton, Electron Spin Resonance (McGraw-Hill Book Company).

29. Bridgman, P. W., Proc. Am. Acad. Arts Sci. 60, 303 (1925).

30. Stockbarger, D. C., Rev. Sci. Instruments 7, 133 (1936).

31. Stockbarger, D. C., Discussion Faraday Soc. 5, 294, 299 (1949).

32. Butler, C. T., Ph.D. Thesis, Oklahoma State University (1972).

33. Wolf, M. W., Ph.D. Thesis, Oklahoma State University (1974).

34. Kravitz, L. C., and W. W. Piper, Phys. Rev. 146, 322 (1966).

VITA

Kanan Bihari Saha

Candidate for the Degree of

Doctor of Philosophy

Thesis: MAGNETIC RESONANCE STUDY OF POINT DEFECTS IN $KMgF_3$ and $RbMgF_3$

Major Field: Physics

Biographical:

Personal Data: Born at Jiaganj, West Bengal, India, July 31, 1938, the son of Basanta K. and Jugal R. Saha.

Education: Graduated from R. V. S. Vidyamandir, Jiaganj, India in 1955; received B.S. (Honors) 1950 and M.S. (Physics) 1962 from University of Calcutta; received M.S. in Physics from Cleveland State University in 1972; completed the requirements for the degree of Doctor of Philosophy at Oklahoma State University, Stillwater, Oklahoma, in July, 1978.

Experience: Physics Teacher, Dinabandhu Andrews College, Garia, Calcutta, India (1963-1970); optical benchman, State Optical Co., Inc., Cleveland, Ohio (1970-1972); Graduate Teaching and Research Assistant, Oklahoma State University, Stillwater, Oklahoma, 1973-1978.